Supplementary Information (SI) for Journal of Materials Chemistry A.

Supporting information

Integrated Multiscale Structural Engineering of Fe–N–C Electrocatalysts and Device Components for High-Performance PEMFCs

Seung Yeop Yi, Sanghyeok Lee, Jaemin Kim, Jinyeop Kim, Daeeun Choi, Minkyeong Ban, Dongyoon Woo, Hyunwoo Jun, Yeju Jang, Jiyoung An, Wonhyeong Lee, Dong Young Chung, Seoin Back*, Segeun Jang*, Jinwoo Lee*

Contents:

Experimental methods

Supplementary Figures: **S1-S34**

Supplementary Tables: **S1-S8**

Supplementary References

Supporting information

Experimental method

Synthesis of D–Fe–N–C: D–Fe–N–C was synthesized by pyrolysis of the Fe-doped ZIF-8 metal–organic framework to provide a precursor for the atomically dispersed electrocatalysts. Typically, $Zn(NO_3)_2 \cdot 6H_2O$ (23 mmol) and $Fe(NO_3)_3$ 9 H_2O (3 mmol) was dissolved in methanol (150 mL) under sonication to obtain a homogeneous solution (A). In addition, 2-methylimidazole (97 mmol) was dissolved in methanol (150 mL) in a similar manner to obtain a homogeneous solution (B). Subsequently, solution B was poured into solution A and mixed for 20 min. After this time, the reaction mixture vigoruos stirred at room temperature for 24 h to obtain the desired Fe-doped ZIF-8 as a colloidal solution. This colloidal solution was subjected to centrifugation and washed with methanol three times, followed by vacuum drying at 50 °C for 10 h. To synthesize the D–Fe–N–C, the Fe- doped ZIF-8 precursor was placed in a tube furnace and pyrolyzed at 1000 °C (10 °C min^{-1}) for 2 h under a flow of Ar gas (200 sccm).

Synthesis of DM–Fe–N–C: DM–Fe–N–C was synthesized by pyrolysis of the Fe doped Meso ZIF-8 metal–organic framework to provide a precursor for the atomically dispersed electrocatalysts. First, PS_{10k}-b-PEO_{5k} (1 g) was dissolved in tetrahydrofuran (20 ml) under sonication for 10 min to obtain a homogeneous solution (A). $Zn(NO_3)_2 \cdot 6H_2O$ (10 mmol) and Fe $(NO_3)_3 \cdot 9\ H_2O$ (1 mmol) were dissolved in deionized water (250 mL) and poured into solution A. After this time, Solution (B) vigorous stirred for 1hour to forming the micelle. In addition, 2-methylimidazole (15 mmol) was dissolved in deionized water (120 mL) in a similar manner to obtain a homogeneous solution (C). Subsequently, solution C was poured into solution B. The reaction mixture vigorous stirred at room temperature for 24 h to obtain the desired Meso-Fe-doped ZIF-8 as a colloidal solution. This colloidal solution was subjected to centrifugation and washed with methanol and tetrahydrofuran (THF) three times, followed by vacuum drying at 50 °C for 10 h. To synthesize the DM–Fe–N–C, the Meso-Fe-doped ZIF-8 precursor was placed in a tube furnace and pyrolyzed at 1000 °C (10 °C min^{-1}) for 2 h under a flow of Ar gas (200 sccm).

Synthesis of T M–Fe–N–C: M–Fe–N–C was synthesized by pyrolysis of the Meso ZIF-8 metal–organic framework to provide a support material for the atomically dispersed electrocatalysts. To prepare Meso ZIF-8, Fe precursor was excluded with same process descrived above for DM–Fe–N–C. The atomically dispersed M–Fe–N–C electrocatalyst was prepared using a Meso ZIF-NC-based ion adsorption method and thermal activation. Specifically, 500 mg of Meso ZIF-NC was homogeneously dispersed in 40 mL of isopropanol, while $Fe(NO_3)_3{\cdot}9H_2O$ (7.5 mL, 12 mg mL^{-1} in isopropanol) was prepared separately to achieve the desired Fe loading relative to the mass of Meso ZIF-NC. The $Fe\ (NO_3)_3 \cdot 9\ H_2O$ solution was slowly added dropwise to the Meso ZIF-NC solution under vigorous stirring and allowed to continue stirring for 24 h. After this time, the mixed solution was subjected to centrifugation and vacuum drying for 10 h at 60 °C. For thermal activation, the obtained powder was placed in a crucible and annealed specific temperature (700°C - 1000°C) for 2 h with 10 °C min^{-1} ramping rate under a flow of Ar gas (200 sccm).

Materials characterization: Powder X-ray diffraction (XRD) was performed using a Rigaku D/MAX-2500 diffractometer with Cu Kα radiation ($\lambda = 0.1542$ nm) at a scanning speed of 4° per minute. Transmission electron microscopy (TEM) images were obtained with an FEI Tecnai F20 operating at 200 keV, while energy-dispersive X-ray (EDX) mapping was conducted using an FEI Talos F200X under the same voltage. The Brunauer-Emmett-Teller

(BET) surface area was measured at 77 K using a Micromeritics Tristar II 3020 system. X-ray photoelectron spectroscopy (XPS) analysis was carried out with a Kratos Axis-Supra spectrometer employing Al Kα radiation (1486.7 eV). Raman spectra were recorded using a HORIBA LabRAM HR Evolution Visible NIR system with an excitation wavelength of 514 nm. Mössbauer spectroscopy was conducted at 295 K in transmission mode, using a ^{57}Co source embedded in a rhodium matrix. A fixed absorber was utilized in an electromechanical Mössbauer spectrometer operated in constant-acceleration mode, and the data were analyzed using MossWinn 4.0i software.

Electrochemical measurements: Catalyst inks were prepared by dispersing 10 mg of the desired catalyst in a 2 mL mixture containing water (340 µL), isopropanol (1600 µL), and 5 wt% Nafion solution (60 µL). The mixture was ultrasonicated for 1 hour to ensure a homogeneous solution. Before applying the catalyst ink to the rotating disk electrode (RDE), the RDE surface was polished using an alumina suspension. The prepared ink was then deposited onto the RDE surface under rotation at 700 rpm, followed by air drying. The catalyst loading was set at 600 µg cm^{-2} for atomically dispersed Fe–NC electrocatalysts and 100 µg cm^{-2} for Pt/C (20 wt.%, Johnson Matthey Fuel Cells Ltd). ORR performance was evaluated using a CHI 660E potentiostat system (CHI Instruments, Inc.) with a three-electrode configuration. Ag/AgCl (3 M NaCl) served as the reference electrode, and a platinum wire was used as the counter electrode. The ORR polarization curves were obtained through linear sweep voltammetry (LSV) in a 0.5 M H_2SO_4 electrolyte at room temperature (25 °C) with a rotation speed of 900 rpm and a sweep rate of 2 mV s^{-1}. The rotating ring-disk electrode (RRDE) technique was conducted with the catalyst loading was set at 200 µg cm^{-2}. The hydrogen peroxide yield (H_2O_2, %) and electron transfer number (n) were calculated based on disc and ring currents (I_d and I_r, respectively) using current collection efficiency (N = 0.37) of the Pt ring (Equation 1 and 2).

$$H_2O_2(\%) = 200 \times \frac{\frac{I_r}{N}}{I_d + \frac{I_r}{N}} \tag{1}$$

$$n = 4 \times \frac{I_d}{I_d + \frac{I_r}{N}} \tag{2}$$

The current collection efficiency of the Pt ring(N) is 0.37. The ASTs were conducted in O_2-saturated 0.5 M H_2SO_4 by potential cycling between 0.6 V and 1.0 V versus RHE at a sweep rate of 50 mV s^{-1} for 10,000 cycles. The durability of the electrocatalysts was further evaluated through chronoamperometric measurements at 0.85 V versus RHE for 100 hours.

Nitrite stripping for determining the accessible site density and turnover frequency:

The accessible active sites of the atomically dispersed catalysts were quantified through nitrite (NO_2^-) reduction at the Fe centers of the Fe–N_4 sites, leveraging the method outlined by Kucernak et al.[1] Nitrite interacts with Fe centers to form stable compounds, effectively poisoning active sites, making this method ideal for assessing site availability. The site densities and turnover frequencies (TOFs) of the Fe–N_4 sites in Fe–N–C catalysts were determined using Equations (3) and (4).

$$Site\ density\ \left(site\ g^{-1}\right) = \frac{Q_{strip} \times N_A}{n_{strip} \times F \times m_{catal}} \tag{3}$$

$$Turnover\ frequency\ \left(s^{-1}\right) = \frac{n_{strip} \times \Delta j_k\ (mA\ cm^{-2})}{Q_{strip}(C\ g^{-1}) \times L_c(mg\ cm^{-2})} \tag{4}$$

The excess coulometric charge (Q_{strip}) associated with the stripping peak was determined by CV of the nitrite reduction region. In these equations, n_{strip} is the number of transferred electrons per stripped nitrite molecule (i.e., 5), and j_k is the kinetic current density, where $\Delta jk =$

$j_k(unposioned)$-$j_k(poisoned)$. Finally, L_c is the catalyst loading (0.242 mg cm^{-2}) during the nitrite reduction process. Utilization rate of Fe was estimated by comparing the surface-accessible Fe quantified by SD analysis with the total Fe content obtained from ICP-MS measurements.

On-line ICP-MS for determining the quantity of demetallation Fe: In situ dissolution of Fe ions was detected with a PerkinElmer NexION 2000 coupled to a stationary probe rotating disk electrode setup (geometric area: 0.283 cm^2, electrode rotating speed: 100 rpm).[2] The electrolyte (Ar-saturated 0.1 M $HClO_4$) was pumped out with 7.5 μL s-1 of flow rate and fresh electrolyte was restored to the cell with same flow rate to maintain the total volume. The kinetic energy discrimination (KED) mode with helium gas flow was used to improve detection limits for detection of Fe ions (56 and 57 AMU). The catalyst ink, prepared with catalyst powder and Nafion binder in deionized (DI) water and 2-propanol, was applied to a glassy carbon disk and the catalyst loading was 300 μg cm^{-2} for each measurement. Electrochemical measurements were controlled using an Autolab PGSTAT 302N potentiostat, utilizing a conventional three-electrode setup. The counter and reference electrodes were a graphite rod (99.9995%) and Ag/AgCl with a double junction, respectively, housed in a fluoropolymer-based cell. To ensure cleanliness, the cell and the counter electrode were thoroughly rinsed and boiled in DI water before each experiment. Potential sweep (1.0 ~ 0.0 V vs. RHE) was applied for ICP-MS data collection, synchronizing Fe intensity and applied potential with consideration of delay time (8 s) in this setup. Representative Fe dissolution rate for each catalyst was calculated from 56Fe signal after 10 pre-cycles for stabilization of Fe dissolution.

Computational details: We performed density functional theory (DFT) calculations using Vienna Ab Initio Simulation Package (VASP) version 5.4.4.[3] The projector augmented wave

(PAW) pseudopotential method[4] and Perdew-Burke-Ernzerhof (PBE) exchange-correlation functional[5] with Grimme's D3 correction were used. [6, 7] The implicit solvation method was employed using VASPsol to account for solvation effects.[8] The energy convergence tolerance was set to 10^{-4} eV, and the kinetic energy cutoff was set to 400 eV. Monkhorst-pack k-points of (2 × 2 × 1) were sampled for all structures. The Gibbs free energies were obtained by including free energy correction values calculated using the ideal gas (harmonic) approximation for gas (adsorbate) molecules as implemented in Atomic Simulation Environment (ASE). i.e., $\Delta G = \Delta E + \Delta ZPE + \int C_p dT - T\Delta S \ (T = 298\ K)$, where ΔE, ΔZPE, $\int C_p dT$ and $-T\Delta S$ correspond to changes in DFT calculated energy, zero-point energy, enthalpic and entropic contributions, respectively.[9]

The computational hydrogen electrode (CHE) method was employed, which assumes the equivalent chemical potential of a proton-electron pair to that of 0.5H_2(g) *i.e.,* $\mu_{(H^+ + e^-)} = 0.5\mu_{H_2}$. According to the CHE method, $\mu_{(H^+ + e^-)}$ is shifted by $-eU$ as the potential U is applied. The following four proton-electron transfer pathway was considered to evaluate the reaction energetics[10]:

$$* + O_2 + (H^+ + e^-) \rightarrow OOH^* \quad (5)$$

$$OOH^* + (H^+ + e^-) \rightarrow O^* + H_2O \quad (6)$$

$$O^* + (H^+ + e^-) \rightarrow OH^* \quad (7)$$

$$OH^* + (H^+ + e^-) \rightarrow * + H_2O \quad (8)$$

where * denotes the active site. The highest potential at which all the reaction steps become downhill in the Gibbs free energy is defined as the thermodynamic limiting potential (U_L). The limiting potential is evaluated as: $U_L = min(4.92 - \Delta G_{OOH^*}, \Delta G_{OOH^*} - \Delta G_{O^*}, \Delta G_{O^*} - \Delta G_{OH^*}, \Delta G_{OH^*})$. A higher U_L corresponds to higher ORR catalytic activity. All adsorption energies for the intermediates were referenced to H_2O and H_2 molecules. Thus, ΔG_{OOH^*}, ΔG_{O^*}, ΔG_{OH^*} were calculated by the following equations.

$$\Delta G_{OOH^*} = E(OOH^*) + 1.5\mu_{H_2} - E(*) - 2\mu_{H_2O(g)} + G_{corr} \quad (9)$$

$$\Delta G_{O^*} = E(O^*) + \mu_{H_2(g)} - E(*) - \mu_{H_2O(g)} + G_{corr} \quad (10)$$

$$\Delta G_{OH^*} = E(OH^*) + 0.5\mu_{H_2} - E(*) - \mu_{H_2O(g)} + G_{corr} \quad (11)$$

where E, μ, G_{corr} correspond to the DFT energy, the chemical potentials of molecules, and the sum of correction values for the Gibbs free energy of each adsorbate, respectively.

The Crystal Orbital Hamiltonian Population (COHP) analysis was conducted using the Lobster package.[11, 12] A COHP diagram was used to distinguish the bonding and antibonding contributions of the binding between Fe binding site and ORR intermediates, based on density of states calculations. ICOHP indicates the integrated COHP over a range of energies up to the Fermi level. A more positive −ICOHP value indicates a stronger bonding interaction between the Fe atom and the ORR intermediate.

Structure modelling of Fe–N–C Catalysts: We model the mesoporous Fe–NC catalysts using curved structures as follows: First, a unit cell of graphene was relaxed, and the relaxed graphene was repeated 4 times in the *x*-direction. Second, various compressive strains were applied in the x-direction, followed by structure relaxations. Third, the unit cell was repeated 7 times in the y-direction. Fourth, six Carbon atoms were removed, and one Fe atom along with four nitrogen atoms were added. A vacuum layer of 20 Å was added in the z-direction to prevent imaginary interactions between the repeating images [**Fig. S15A**]. After choosing the appropriate curvature, four nitrogen atoms were moved towards or against Fe atom, and then fixed in place to model the Fe–N–C catalysts with local strain applied between Fe and N [**Fig. S15C**].

<u>*Demetallation of Fe from Fe–N$_4$ sites:*</u> We investigated how the local structure affects the stability of Fe–N–C catalysts against demetallation.[13] The stability is evaluated based on the thermodynamic tendency of a single Fe atom to dissolve into the electrolyte.[14] The Fe atom can dissolve into the bulk, becoming an aqueous Fe^{2+} ion, resulting in an $H_2N_4C_{106}$ structure with a metal vacancy. Under reaction conditions, the demetallation reaction can be expressed by the following equation (12).

$$O^*FeN_4C_{106} + 4H^+_{(aq)} \rightarrow Fe^{2+}_{(aq)} + N_4C_{106}H_2 - 2e^- + H_2O \tag{12}$$

Considering $Fe^{2+}_{(aq)} + 2e^- \rightarrow Fe_{(s)}$, the above equation is reorganized as equation (13).

$$O^*FeN_4C_{106} + 4(H^+ + e^-) \rightarrow N_4C_{106}H_2 + Fe + H_2O \tag{13}$$

We then calculated the Gibbs free energy of Fe^{2+} using the DFT energy of the bulk Fe and the standard reduction potential.

$$G(Fe^{2+}) = E_{DFT}\,(Fe_{bulk}) + \Delta G_{diss} \tag{14}$$

$$\Delta G = 2E^{\circ} + 0.0592\log\left[Fe^{2+}\right] \tag{15}$$

Here, $E_{DFT}\,(Fe_{bulk})$ is the DFT energy of the bulk Fe. ΔG_{diss} is the reaction Gibbs free energy of the Fe dissolution, where the standard reduction potential of Fe^{2+}/Fe is -0.44 V and the approximate concentration is assumed to be $10^{-6}\,M$ for a dissolved metal ion.[15]

Thus, the overall Gibbs free energy change of the demetallation is expressed as equation (16).

$$\Delta G_{demetal} = G\left(Fe^{2+}_{(aq)}\right) + G\left(N_4C_{106}H_2\right) + G\left(H_2O\right) - G\left(O^*FeN_4C_{106}\right) - 2 \times G\left(H_2\right) \quad (16)$$

Fabrication of P-G-Ni Foam: A Ni foam (MTI Korea Co., Ltd., Korea) with a purity greater than 99.96%, a thickness of 1.6 mm, a surface density of 42 mg cm-2, and a porosity of 75 pores per inch (PPI) was used in this study. Graphene was coated onto the Ni foam substrate using a thermal CVD process (Charmgraphene Co., Ltd, Korea). To grow graphene, the temperature of the cold-wall CVD chamber was raised to approximately 1020 °C, and methane, hydrogen, and argon were supplied at flow rates of 50 sccm, 20 sccm, and 100 sccm, respectively, under a pressure of 5.5 torr for 1 hour. After the growth process, gas flow was stopped, and the system was rapidly cooled to room temperature. To further enhance the hydrophobicity of the surface of the G-Ni foam, poly (3,3,4,4,5,5,6,6,7,7,8,8,9,9,10,10,10-heptadecafluorodecyl methacrylate, PFDMA) was deposited using an iCVD equipment (D4L-iH2 Model, Deepsmartech Co., Ltd, Korea). The monomer, PFDMA (Merck), and the initiator, tert-butyl peroxide (TBPO, Merck), were vaporized and introduced into the iCVD reactor. To supply the materials to the reactor, the canisters containing the monomer and initiator were heated to 65 °C and 35 °C, respectively. The substrate temperature and chamber pressure were maintained at 30 °C and 100 mTorr, respectively, while the filament temperature was set to 250 °C to activate the initiator. Finally, a poly (PFDMA) thin film of approximately 20 nm was coated on both sides of the G-Ni foam.

Preparation of MEA: Catalyst ink was prepared by dispersing the catalyst and 5wt.% Nafion ionomer (EW725, 3M, USA) in a mixed solvent of DI water and IPA. The Nafion ionomer was added at a ratio of 40 wt.% relative to the catalyst. To ensure uniform dispersion, 3 mm zirconia balls were added, and ball milling was performed at 200 rpm for 12 hours. Afterward, the zirconia balls were removed, and the ink was further dispersed using an ultrasonic process. The prepared catalyst ink was spray-coated onto a Nafion 211 membrane (Dupont, USA) with a reaction area of 5 cm^2. Finally, a PGM-free catalyst was deposited on the cathode side with a loading of 3 mg cm^{-2}. For the anode, a Pt/C catalyst (46.9 wt.% Pt, Tanaka, Japan) was deposited with a Pt loading of 0.1 mg_{Pt} cm^{-2}, maintaining an ionomer-to-carbon ratio of 0.5. The coating method for the anode was the same as that used for the cathode.

Performance and Durability of Single-cell: The fabricated catalyst-coated membrane (CCM) was sandwiched between gas diffusion layers (GDLs, Sigracet 39BB, Germany). A serpentine-type graphite flow field or P-G-Ni foam was used on the cathode side, while a serpentine-type graphite flow field was consistently used on the anode side. We designed the flow field for Ni foam with a depth of 0.5 mm (**Fig. S26B**) so that the Ni foam (original thickness: 1.6 mm) would reach this final thickness after cell assembly. To prevent damage to the GDL and MEA, the Ni foam was pre-compressed from 1.6 mm to 0.6 mm prior to use. As shown in **Fig. S38**, the pressure drop between the inlet and outlet was measured, and the 0.5 mm configuration exhibited almost no additional pressure drop, showing values comparable to those of the serpentine graphite channel. Therefore, this compression ratio was selected as the optimal condition. The assembled cell was evaluated for electrochemical performance and durability using a fuel cell test station (CNL Energy, Korea) and an impedance analyzer (HCP-803, BioLogic, France). Before performance measurements, fully humidified nitrogen gas was supplied to the anode and cathode at 500 mL min^{-1} under 1 bar backpressure while maintaining the cell temperature at 80 °C to ensure sufficient hydration of the electrolyte membrane. To prevent flooding, RH was adjusted to 95%, and H_2 (300 mL min^{-1})/O_2 or Air (1000 mL min^{-1}) was supplied at 1 bar backpressure. At this time, the backpressure of 1 bar is based on gauge pressure. Polarization curves were obtained by decreasing the voltage stepwise from OCV to 0.7 V in 25 mV intervals and from 0.7 V to 0.2 V in 50 mV intervals, measuring the stabilized current density at each point after 20 seconds. Electrochemical impedance spectroscopy (EIS) was conducted at 0.4 V with an AC amplitude of 10 mV and a frequency range of 100 mHz to 100 kHz to compare mass transport characteristics. To measure oxygen transport resistance, hydrogen (1000 mL min^{-1}) to the anode and diluted oxygen gas (3000 mL min^{-1}) to the cathode were used, and the pressure was adjusted to measure the limiting current density. The total oxygen transport resistance (R_t) was calculated using the following equation 17:[16]

$$R_t = 4F\frac{X_{O_2}P - P_W}{j_{lim}\quad RT} \tag{17}$$

Where F is the Faraday constant, X_{O_2} is the oxygen mole fraction, j_{lim} is the limiting current density, P is the total gas pressure, P_W is the vapor pressure, R is the gas constant, and T is the cell temperature. For P_W, a vapor pressure corresponding to 71.5 °C was applied, assuming an 80 °C cell temperature and 70% RH for the oxygen gas to prevent flooding.

To evaluate the durability of the fabricated catalyst, a square-wave cycling test was conducted 30,000 cycles between 0.6 V and OCV under fully humidified H_2 (500 mL min^{-1})/Air (500 mL min^{-1}) at 150 kPa absolute pressure and 80 °C. Cyclic voltammetry (CV) was recorded during the cycling test by supplying fully humidified H_2 (100 mL min^{-1})/N_2 (100 mL min^{-1}) at 80 °C with a scan rate of 20 mV s^{-1}. The electrochemical capacitance (C) was calculated using the following equation 18:[17]

$$C = \frac{\int_{E_1}^{E_2} i dE}{2v(E_2 - E_1)} \tag{18}$$

Where v is the potential scan rate, i is the current density measured during CV, and E_1 and E_2 are the lower and upper potential limits of the CV, respectively. Lastly, the constant-voltage durability test of the MEA was conducted at 0.5 V for 100 hours under the same conditions as the H_2-Air polarization test.

Supplementary Figures

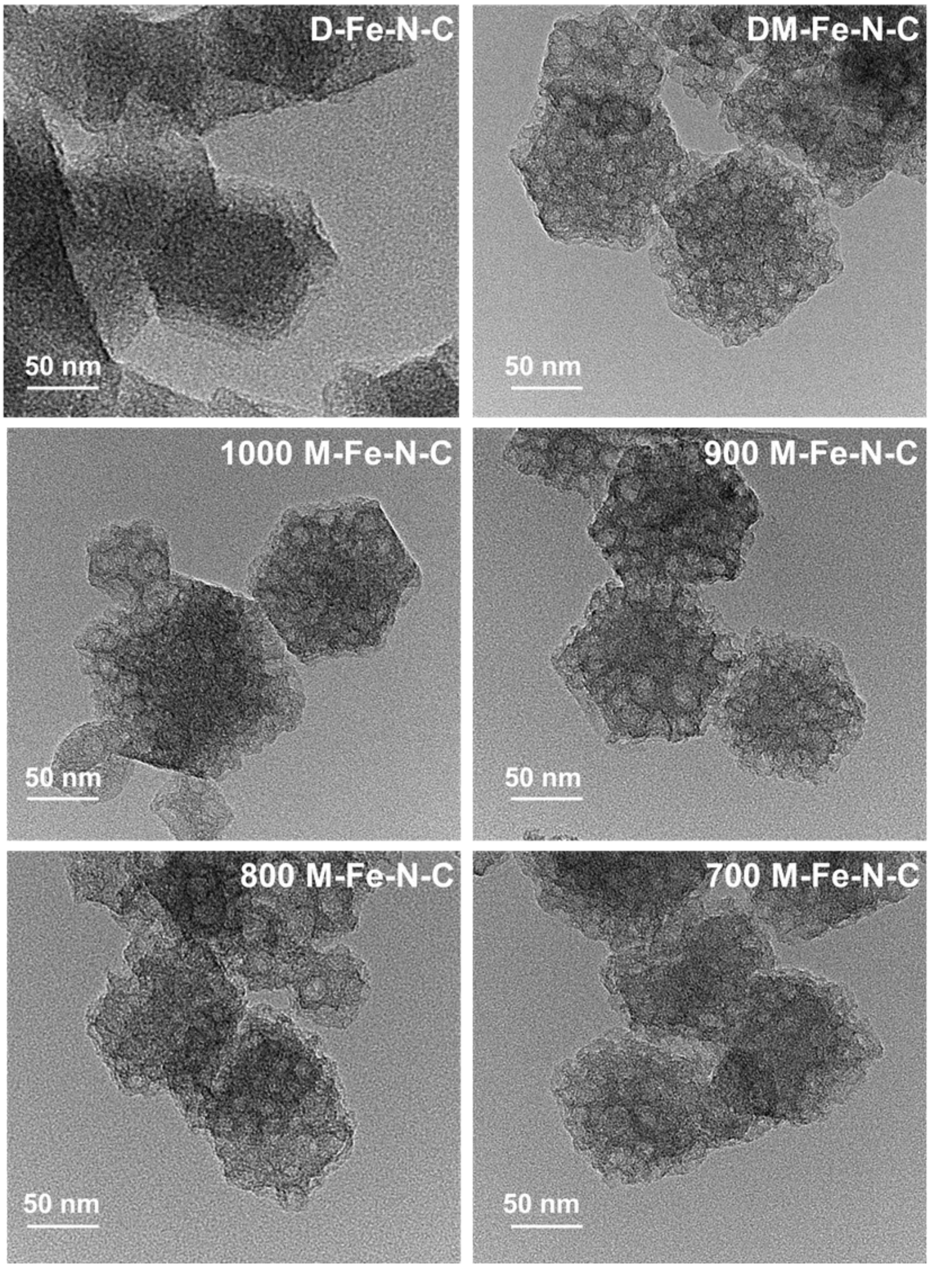

Fig. S1 TEM images of Fe–N–C catalysts

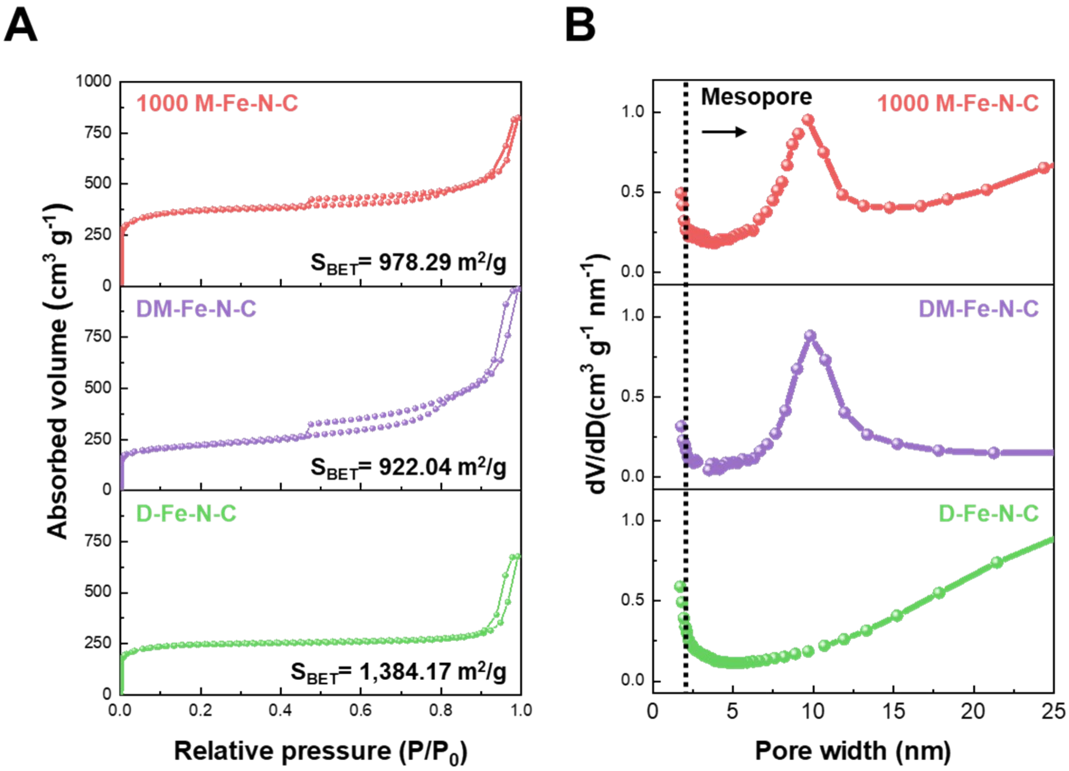

Fig. S2 (A) N_2 adsorption and desorption isotherms and (B) pore size distributions for D–Fe–N–C, DM–Fe–N–C and 1000 M–Fe–N–C.

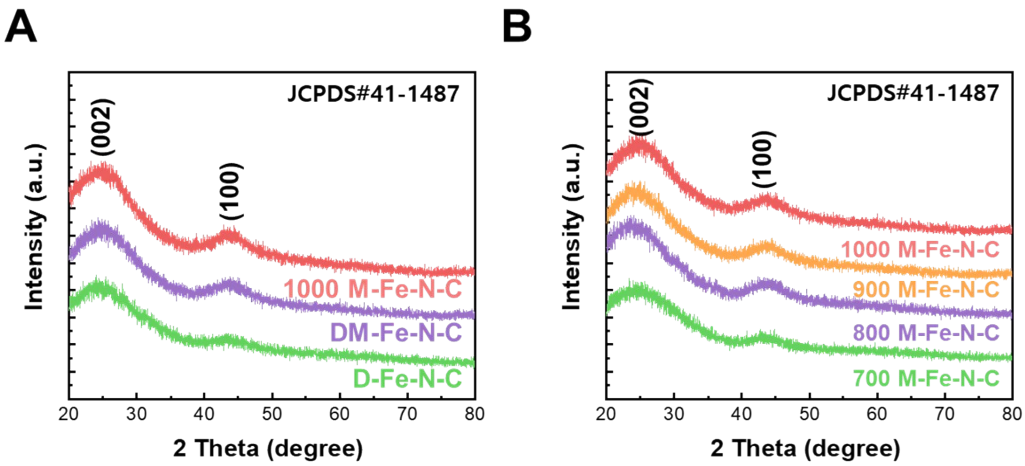

Fig. S3 XRD patterns of (A) Fe–N–C catalysts with different pore structures and (B) M–Fe–N–C electrocatalysts prepared at varying activation temperatures.

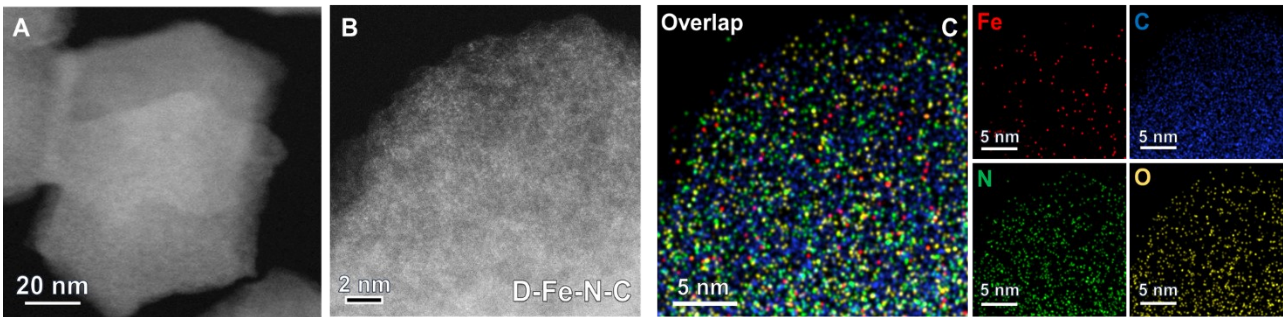

Fig. S4 (A) STEM image. (B) Aberration–Corrected HAADF-STEM image. (C) HAADF-STEM and corresponding elemental EDS mapping images showing the distribution of iron (red), carbon(blue), nitrogen (green) and oxygen elements of D–Fe–N–C.

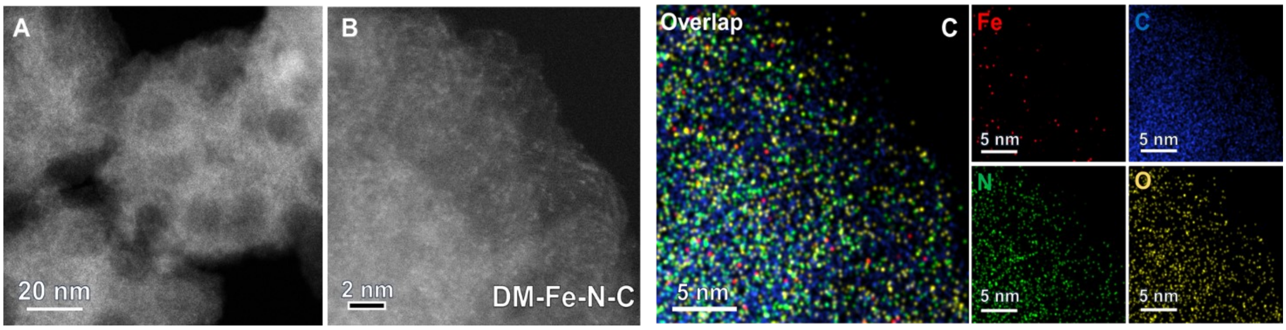

Fig. S5 (A) STEM image. (B) Aberration–Corrected HAADF-STEM image. (C) HAADF-STEM and corresponding elemental EDS mapping images showing the distribution of iron (red), carbon(blue), nitrogen (green) and oxygen elements of DM–Fe–N–C.

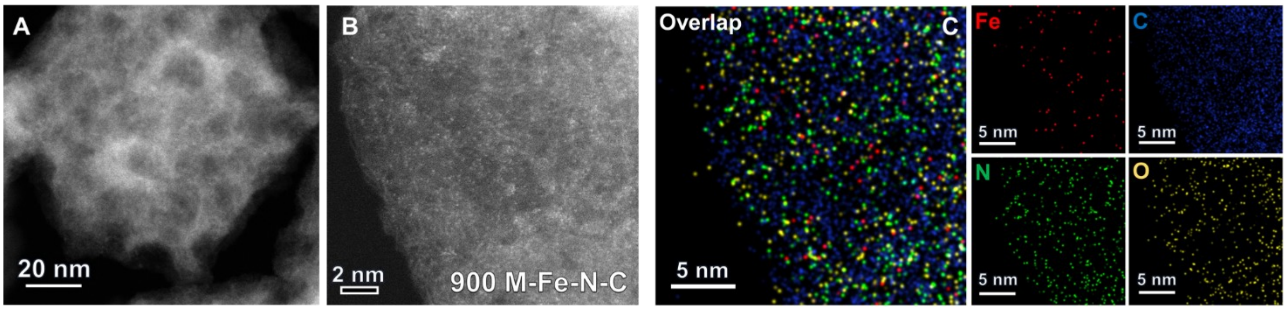

Fig. S6 (A) STEM image. (B) Aberration–Corrected HAADF-STEM image. (C) HAADF-STEM and corresponding elemental EDS mapping images showing the distribution of iron (red), carbon(blue), nitrogen (green) and oxygen elements of 900 M–Fe–N–C.

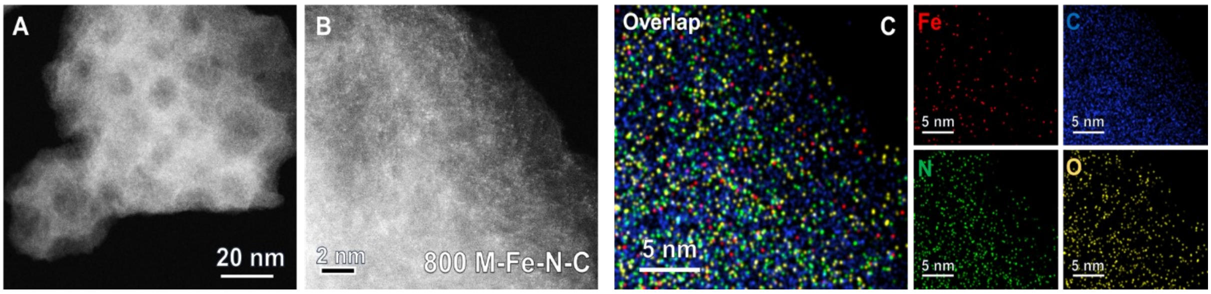

Fig. S7 (A) STEM image. (B) Aberration–Corrected HAADF-STEM image. (C) HAADF-

STEM and corresponding elemental EDS mapping images showing the distribution of iron (red), carbon(blue), nitrogen (green) and oxygen elements of 800 M–Fe–N–C.

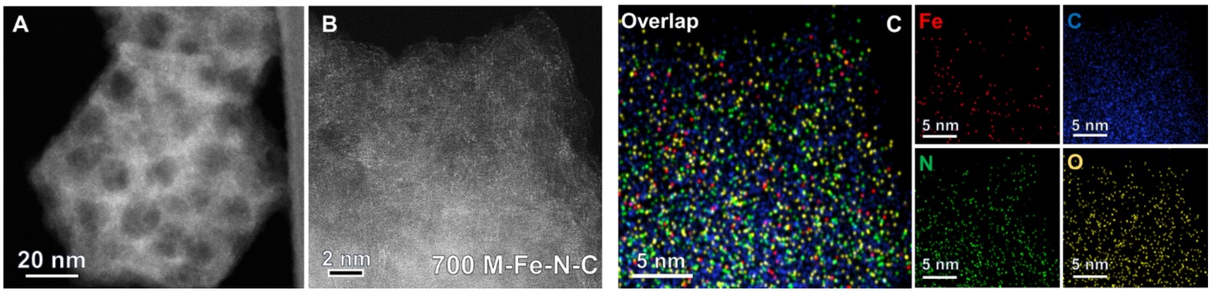

Fig. S8 (A) STEM image. (B) Aberration–Corrected HAADF-STEM image. (C) HAADF-STEM and corresponding elemental EDS mapping images showing the distribution of iron (red), carbon(blue), nitrogen (green) and oxygen elements of 700 M–Fe–N–C.

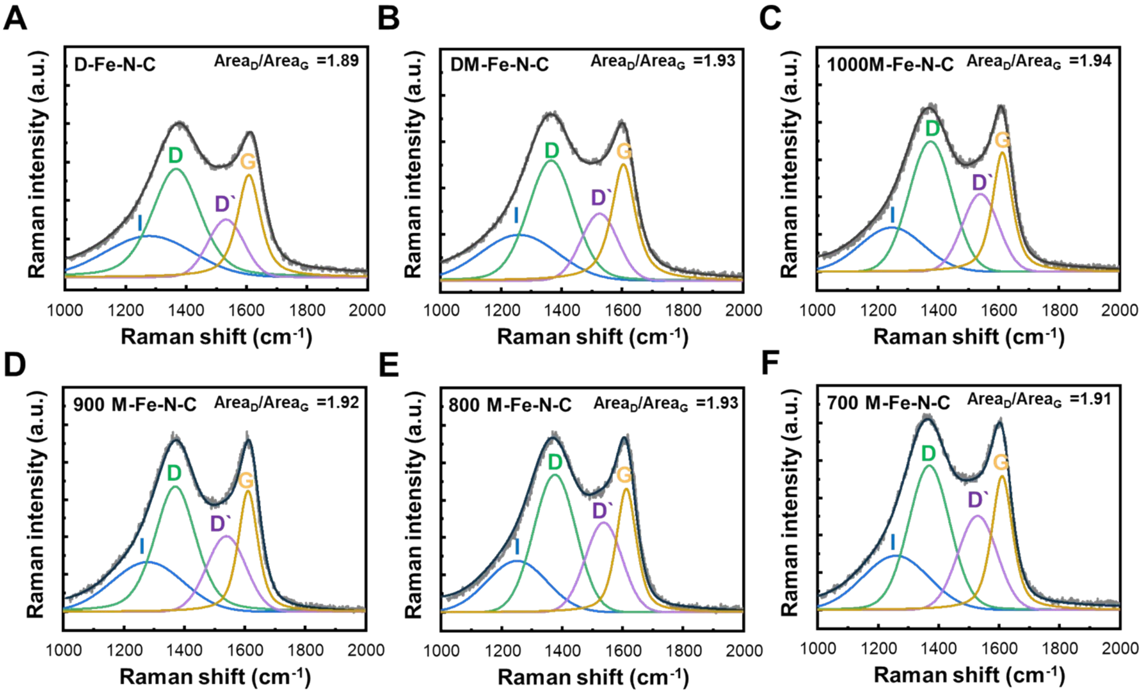

Fig. S9 Raman spectra of (A) D–Fe–N–C, (B) DM–Fe–N–C, (C) 1000 M–Fe–N–C, (D) 900 M–Fe–N–C, (E) 800 M–Fe–N–C and (F) 700 M–Fe–N–C.

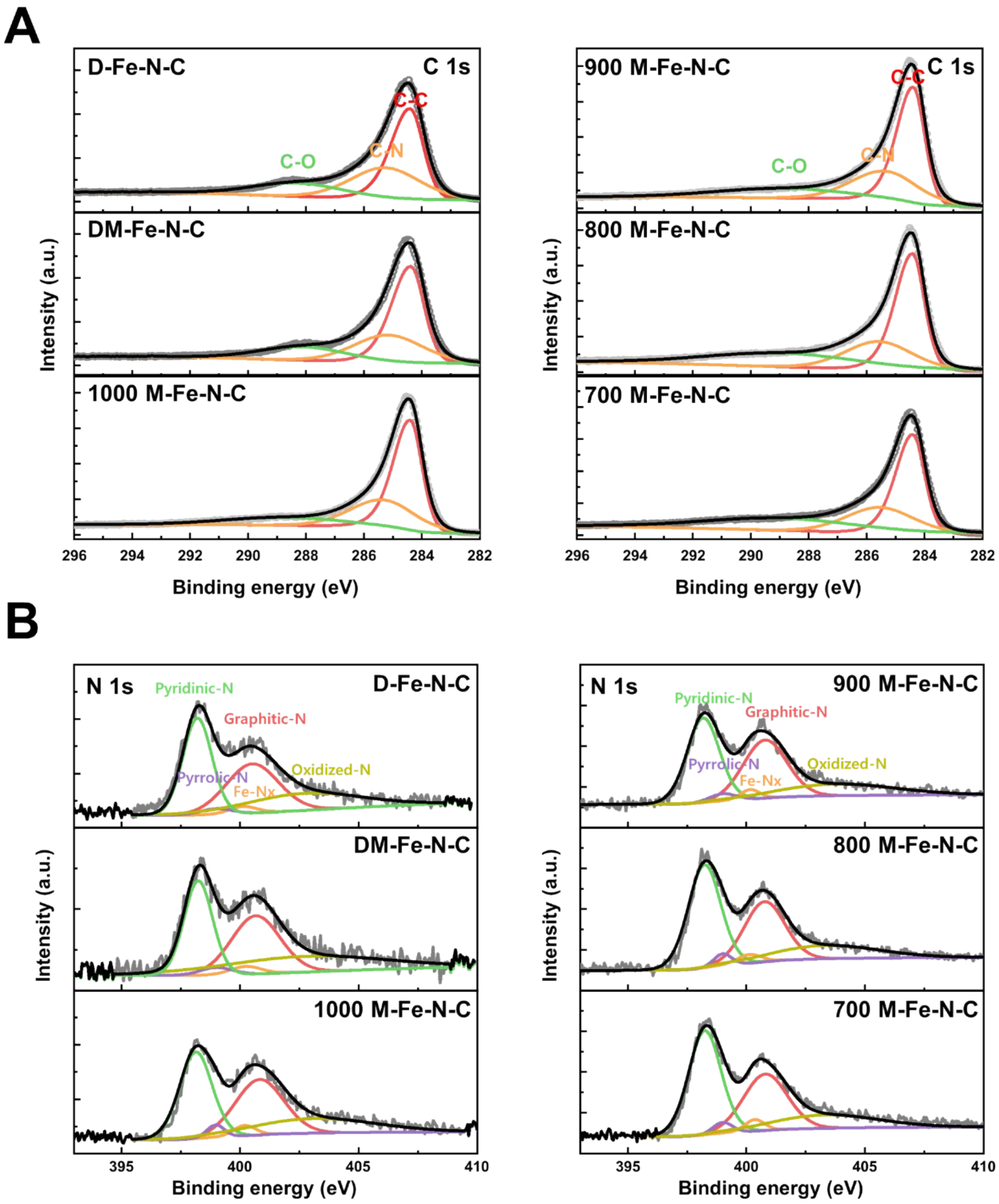

Fig. S10 (A) C 1s and (B) N 1s XPS spectra of Fe–N–C catalysts.

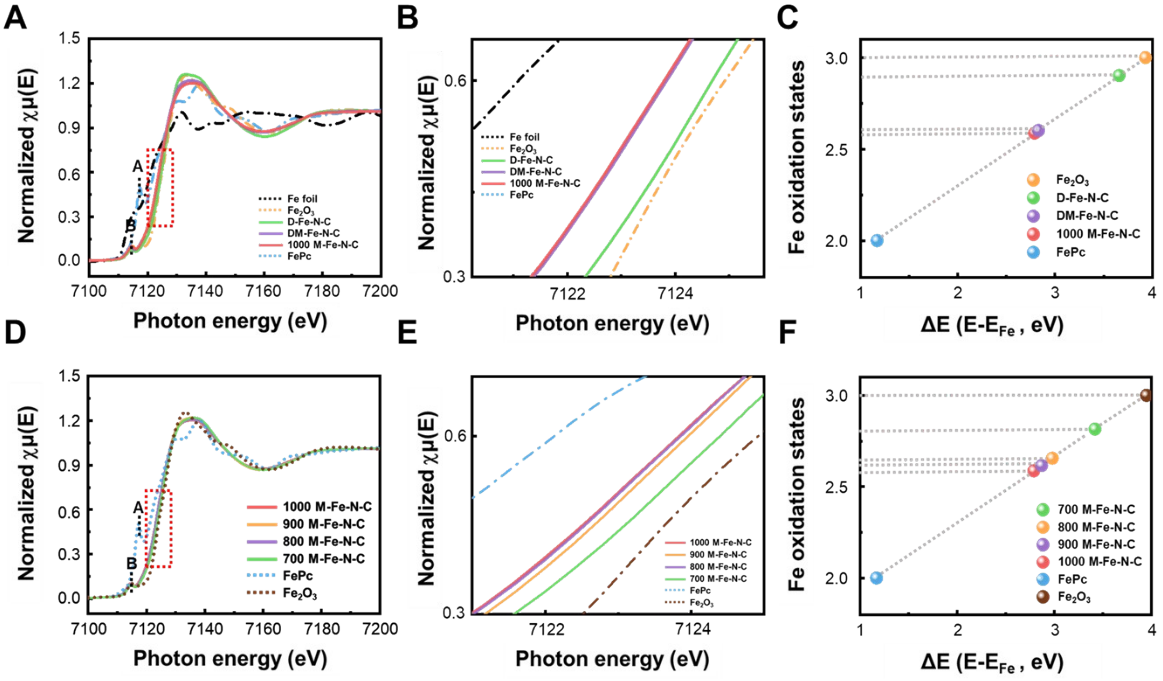

Fig. S11 (A) Fe K-edge XANES spectra, (B) enlarged view and (C) the average oxidation states of Fe center from XANES spectra for D–Fe–N–C, DM–Fe–N–C and 1000 M–Fe–N–C and iron related reference materials (D) Fe K-edge XANES spectra, (E) enlarged view and (F) the average oxidation states of Fe center from XANES spectra for M–Fe–N–C catalysts.

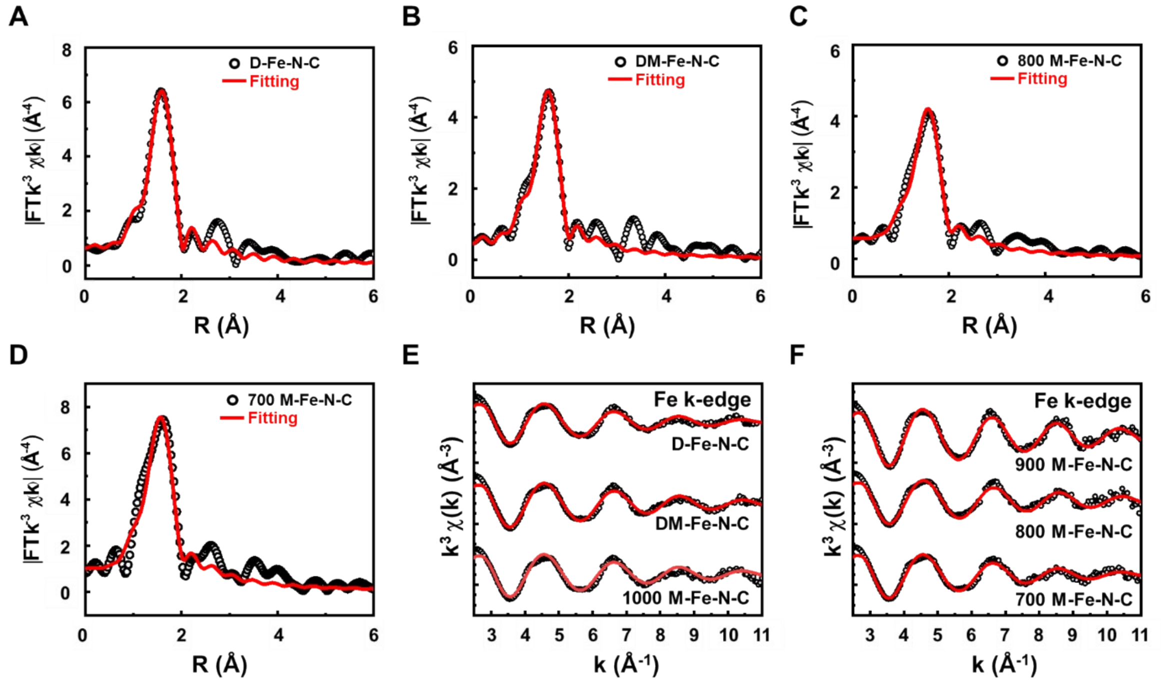

Fig. S12 Fitting for Fe-K edge EXAFS spectra of (A) D–Fe–N–C, (B) DM–Fe–N–C, (C) 800 M–Fe–N–C and (D) 700 M–Fe–N–C. The Table S4 was shown the fitting parameters and results of Fe–N–C catalysts. The first coordination shell of Fe–N–C could be fitted by, with coordination numbers about 5. These results indicate that the Fe center in Fe–N–C catalysts have FeN_4O_1 moiety configuration. The O ligand was probably adsorption of O_2 with exposing the air. k-space spectra of (E) Fe–N–C catalysts synthesized with different pore structures and active site formation methods, and (F) M–Fe–N–C catalysts annealed at different temperatures.

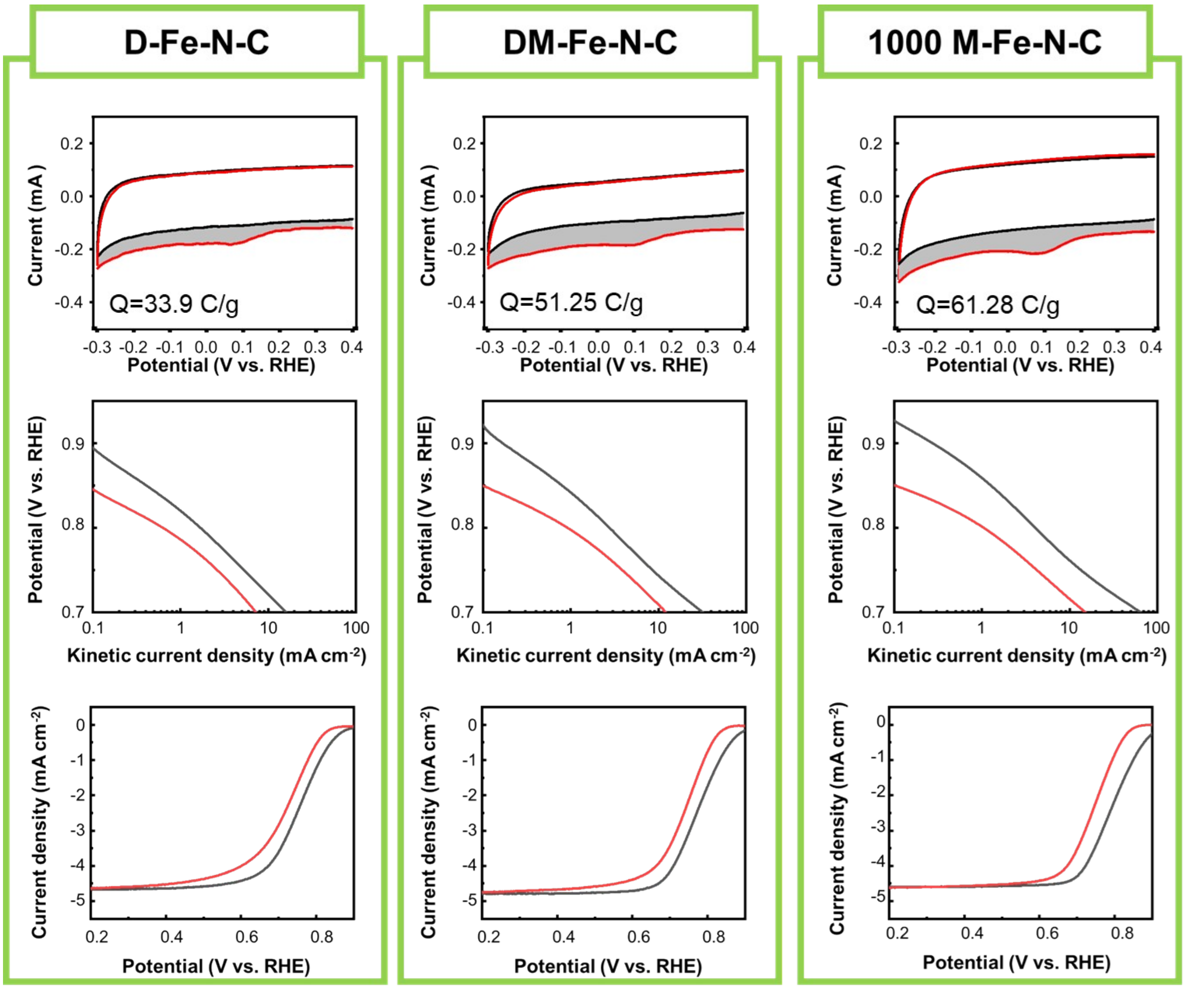

Fig. S13 Determination site density and turnover frequency of D–Fe–N–C, DM–Fe–N–C and 1000 M–Fe–N–C catalysts. The graphs of the first row were CV curves before and after nitrite adsorption in the nitrite reductive stripping region. In middle row, kinetic current density before and after nitrite adsorption. In third row, LSV curves before and after nitrite adsorption in a 0.5 M acetate buffer at pH 5.2.

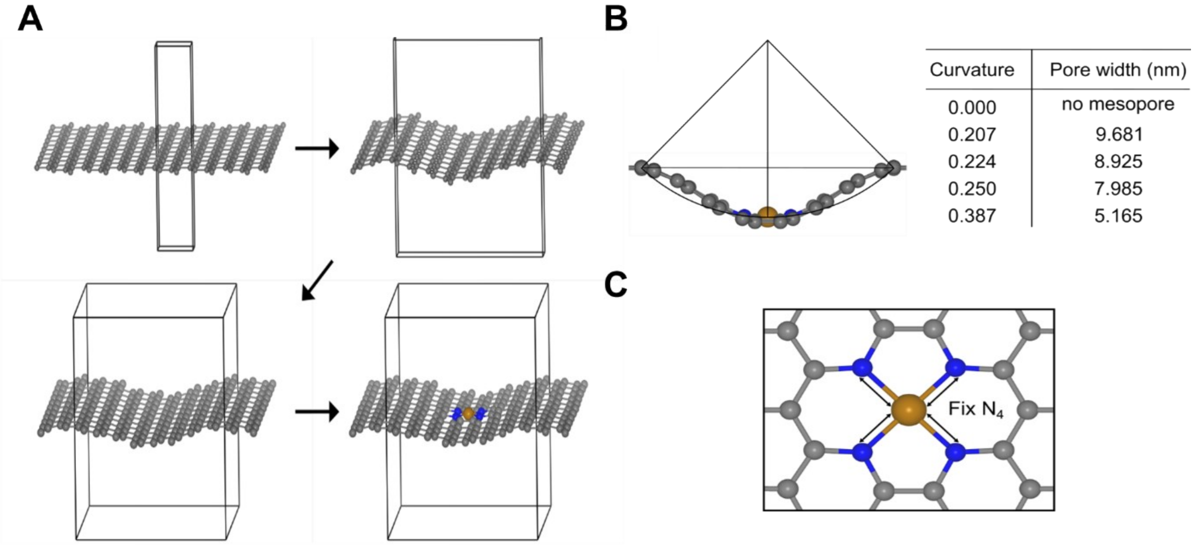

Curvature	Pore width (nm)
0.000	no mesopore
0.207	9.681
0.224	8.925
0.250	7.985
0.387	5.165

Fig. S14 (A) Structure modelling procedure for mesoporous Fe–N–C catalysts. (B) Curvature estimation of the optimized Fe–N–C structure using an ideal spherical model. Based on the experimental observation of semi-spherical mesopores, an ideal spherical geometry was employed to approximate the local curvature. The mesopore diameter, corresponding to the pore width, was estimated from the height difference between the Fe atom and the adjacent C atoms, and the curvature was defined as the reciprocal of the sphere radius. (C) Structure modeling for Fe–N–C catalysts with local strain. To account for varying Fe–N bond lengths, the positions of four nitrogen atoms were adjusted and then fixed in place for subsequent calculations.

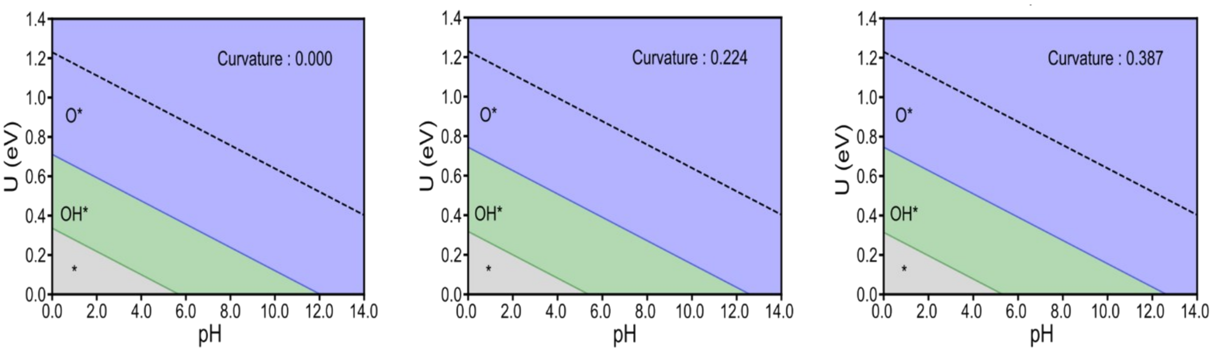

Fig. S15 The surface Pourbaix diagrams of Fe–N–C catalysts with various curvature values. *, OH* and O* in the figure indicate the most stable states under the given conditions. The O* adsorbate was found to be most stable under ORR conditions in all cases.

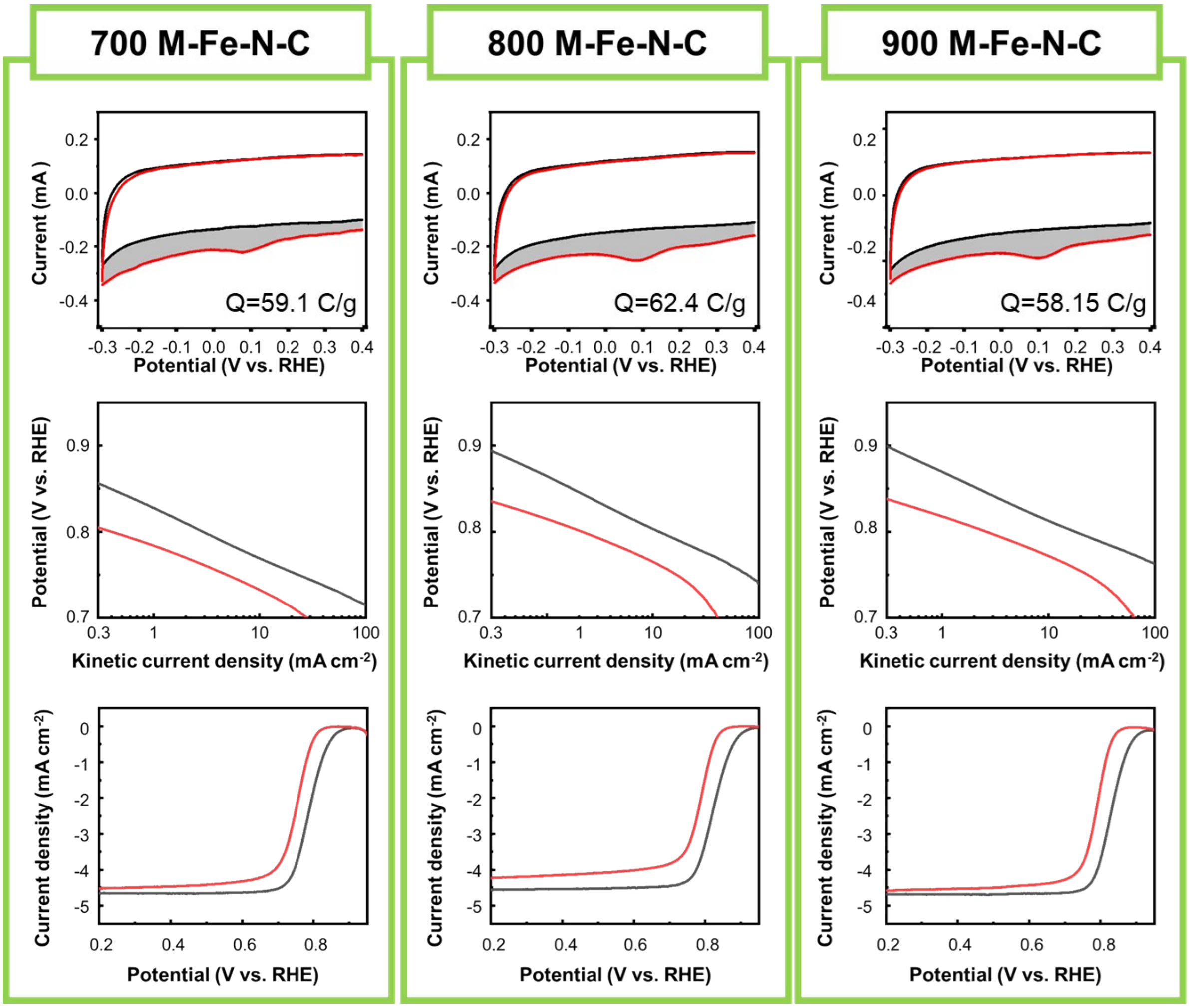

Fig. S16 Determination site density and turnover frequency of 700 M–Fe–N–C, 800 M–Fe–N–C and 900 M–Fe–N–C catalysts. The graphs of the first row were CV curves before and after nitrite adsorption in the nitrite reductive stripping region. In middle row, kinetic current density before and after nitrite adsorption. In third row, LSV curves before and after nitrite adsorption in a 0.5 M acetate buffer at pH 5.2.

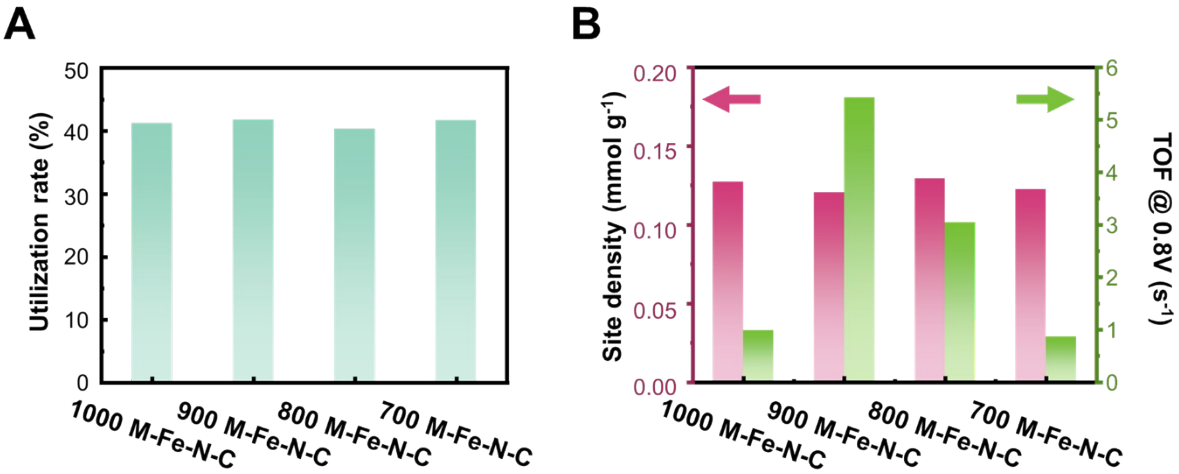

Fig. S17 (A) The utilization rate (B) The comparisons in site density and turnover frequency at 0.8 V_{RHE} for M–Fe–N–C catalysts.

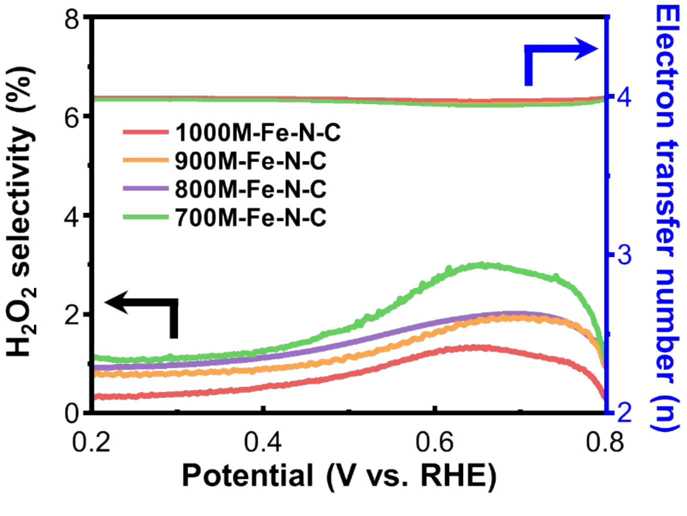

Fig. S18 Selectivity of H_2O_2 and number of transferred electrons (n) of M–Fe–N–C catalysts with a loading of 200 µg/cm².

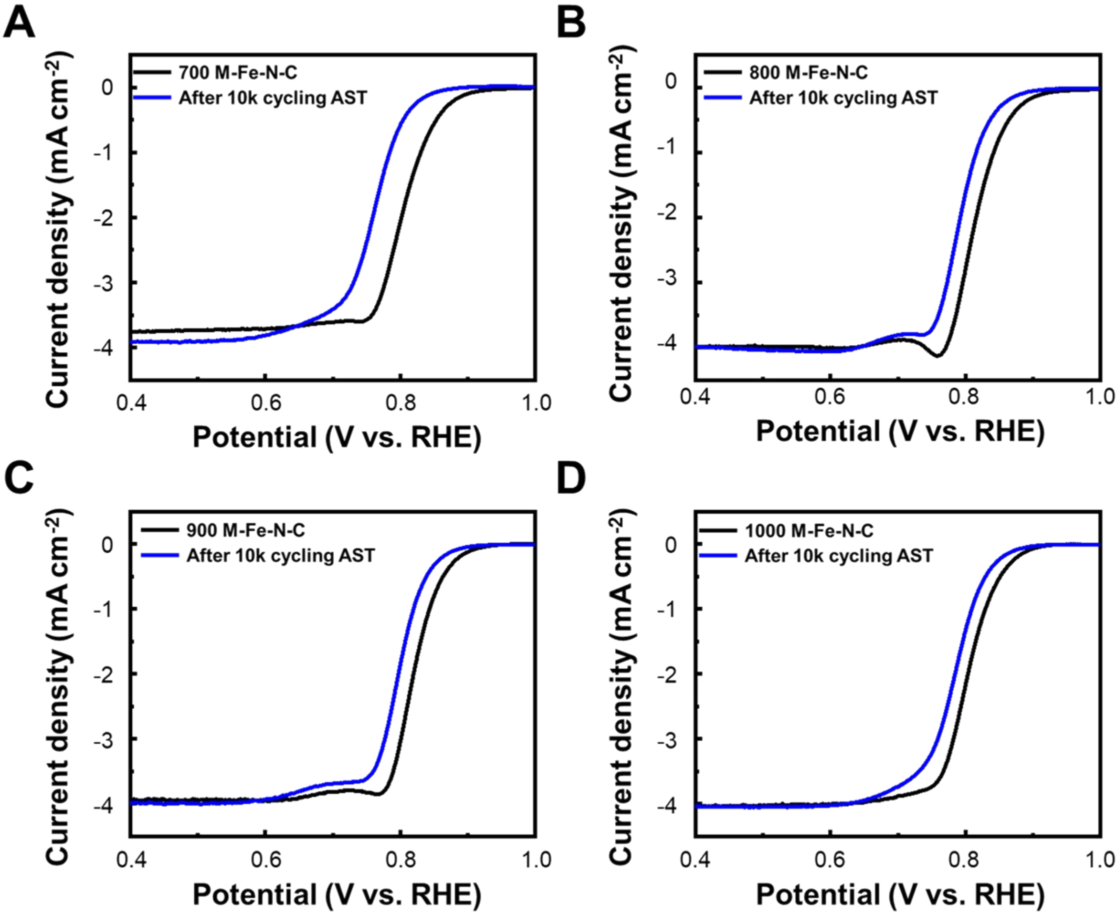

Fig. S19 Polarization curves of M–Fe–N–C catalysts with varying activation temperatures, measured before and after 10k cycles of accelerated stability testing (AST) in the potential range of 0.6 V to 1.0 V.

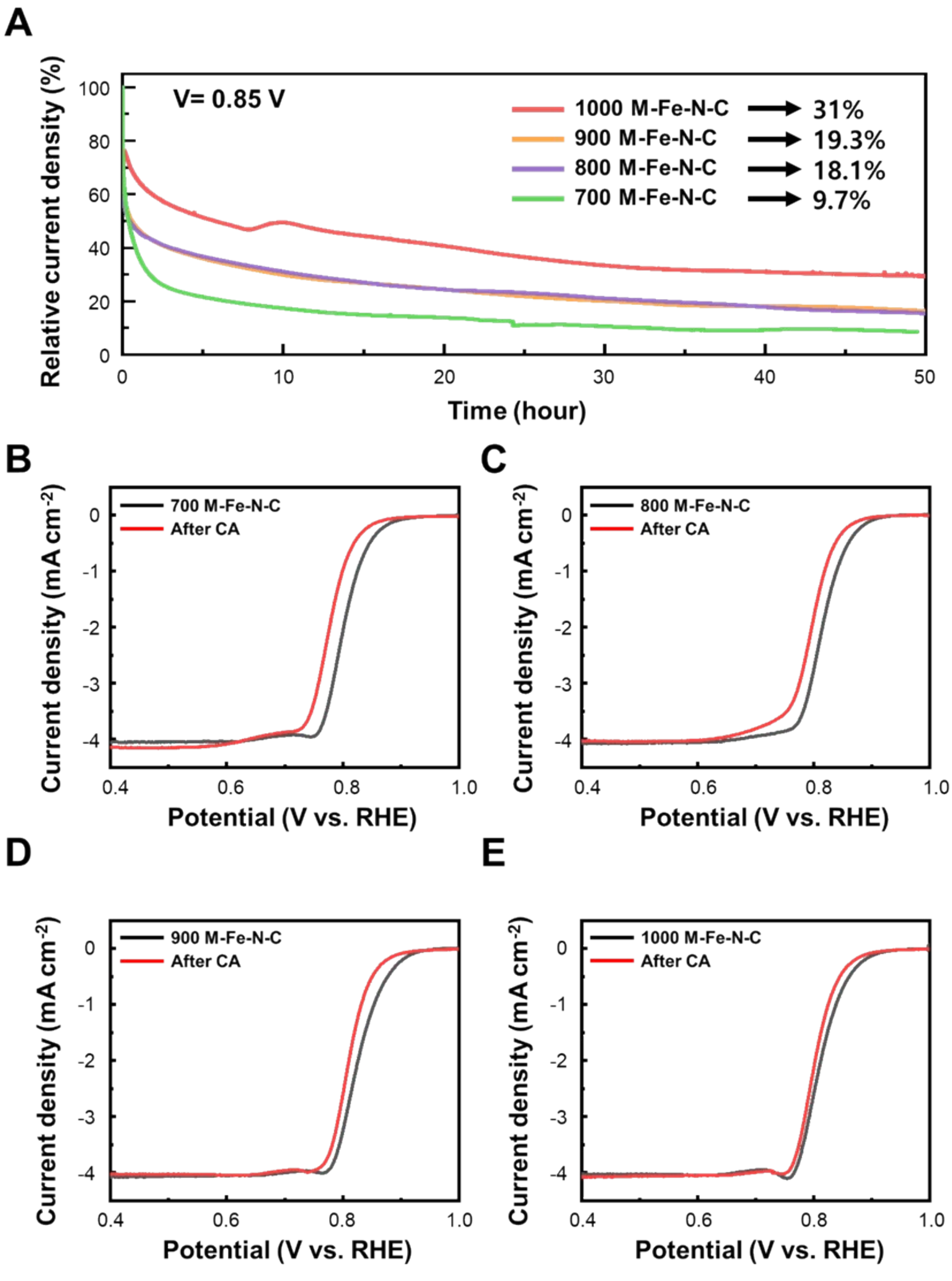

Fig. S20 (A) Chronoamperometry of M–Fe–N–C catalysts at 0.85 V. B-E) Polarization curves of M–Fe–N–C catalysts prepared at varying temperatures: (B) 700°C, (C) 800°C, (D) 900°C, and (E) 1000°C, measured before and after the chronoamperometry test conducted at 0.85 V.

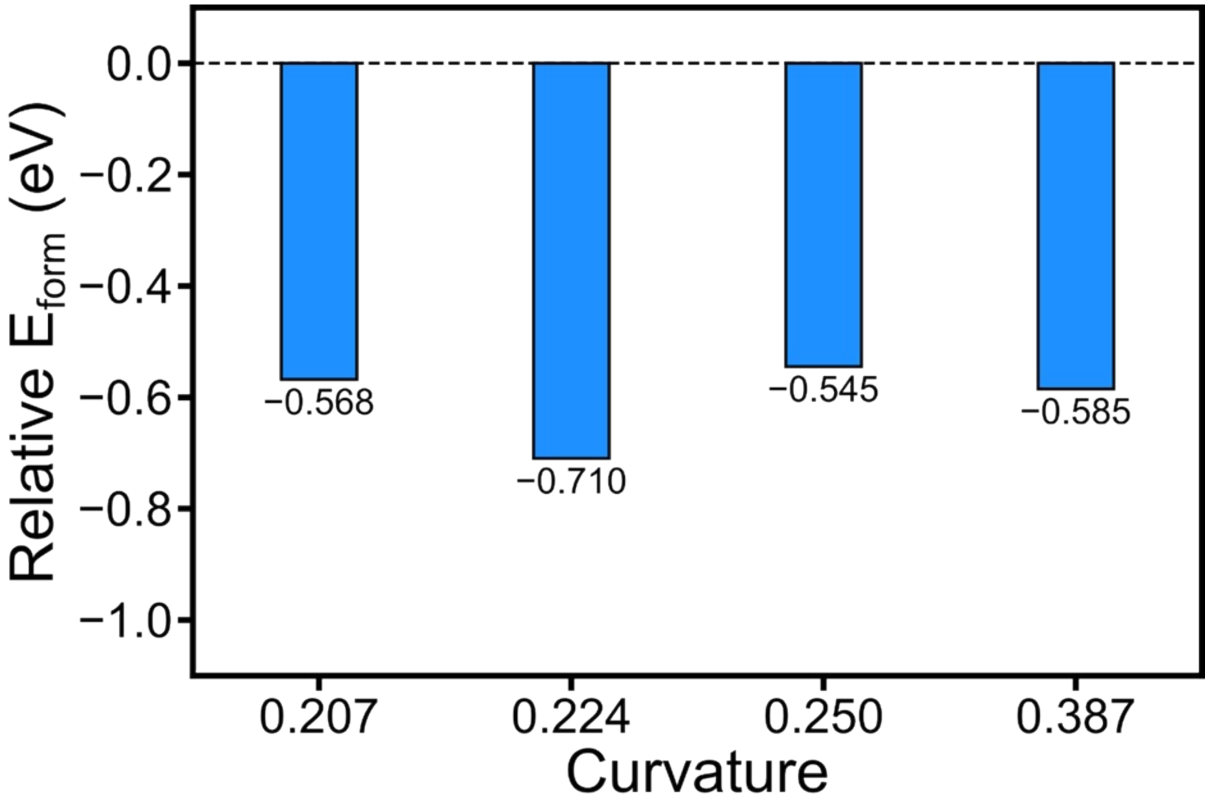

Fig. S21 The relative formation energy of Fe–N–C for different curvature values with respect to pristine Fe–N–C, which was calculated as $E_{DFT}(Fe-NC_{curved}) - E_{DFT}(Fe-NC_{pristine})$.

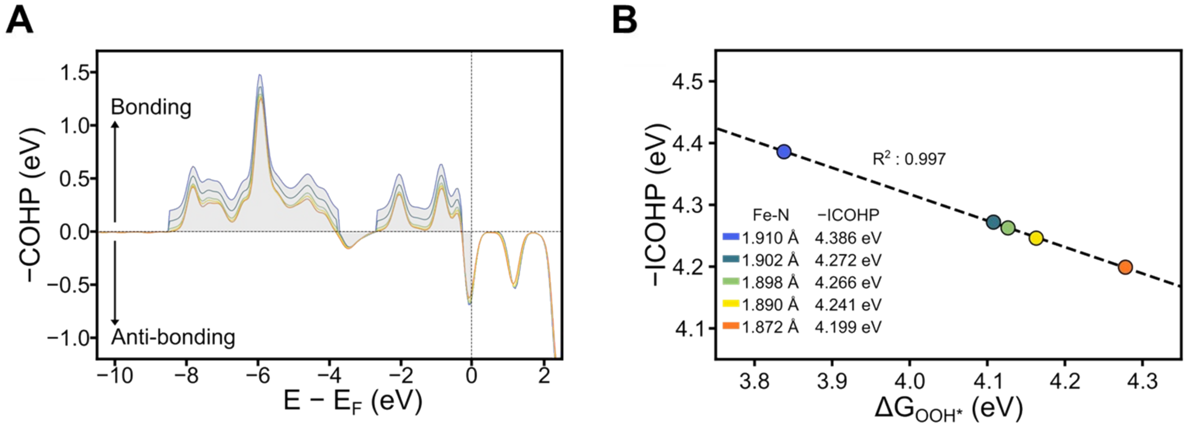

Fig. S22 (A) The COHP plots for Fe-OOH* bonding. A negative COHP indicates bonding interactions, while positive COHP indicates antibonding interactions. (B) The linear correlation between −ICOHP and ΔG_{OOH^*}.

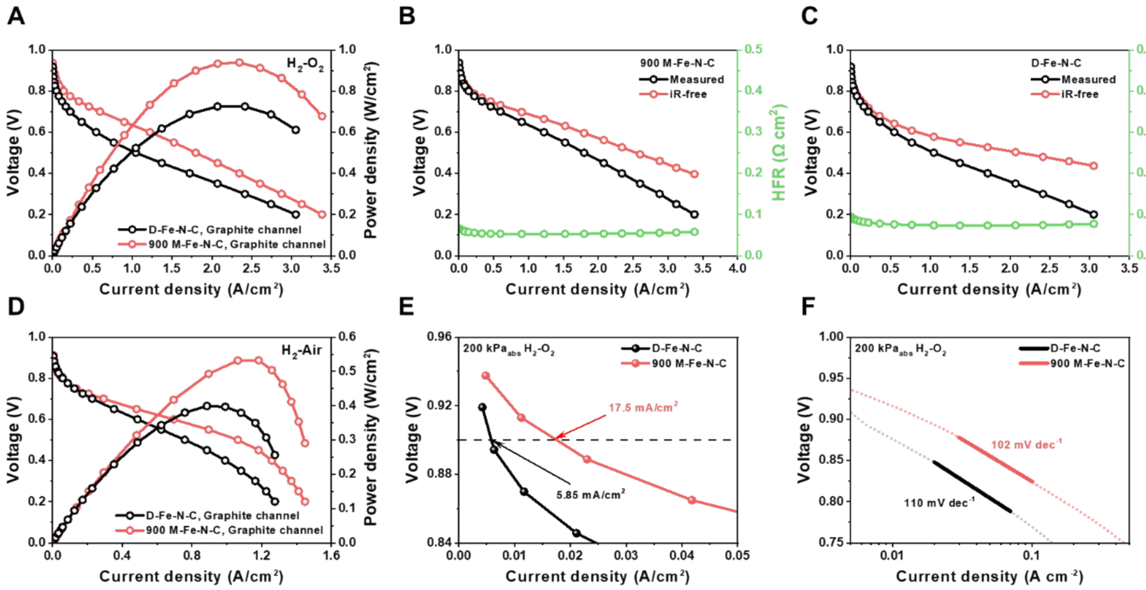

Fig. S23 (A) Polarization curves of the MEAs with D–Fe–N–C and 900 M–Fe–N–C at 80°C supplied with H_2/O_2 at 95% RH. (B) H_2-O_2 polarization curves of 900 M–Fe–N–C with iR-free. (C) H_2-O_2 polarization curves of D–Fe–N–C with iR-free. (D) Polarization curves of the MEAs with D–Fe–N–C and 900 M–Fe–N–C at 80°C supplied with H_2/air at 95% RH. (E) Current densities at 0.9 V on the iR-free polarization curves. (F) Tafel plots of the iR-free voltages under 1 bar H_2/O_2 environment.

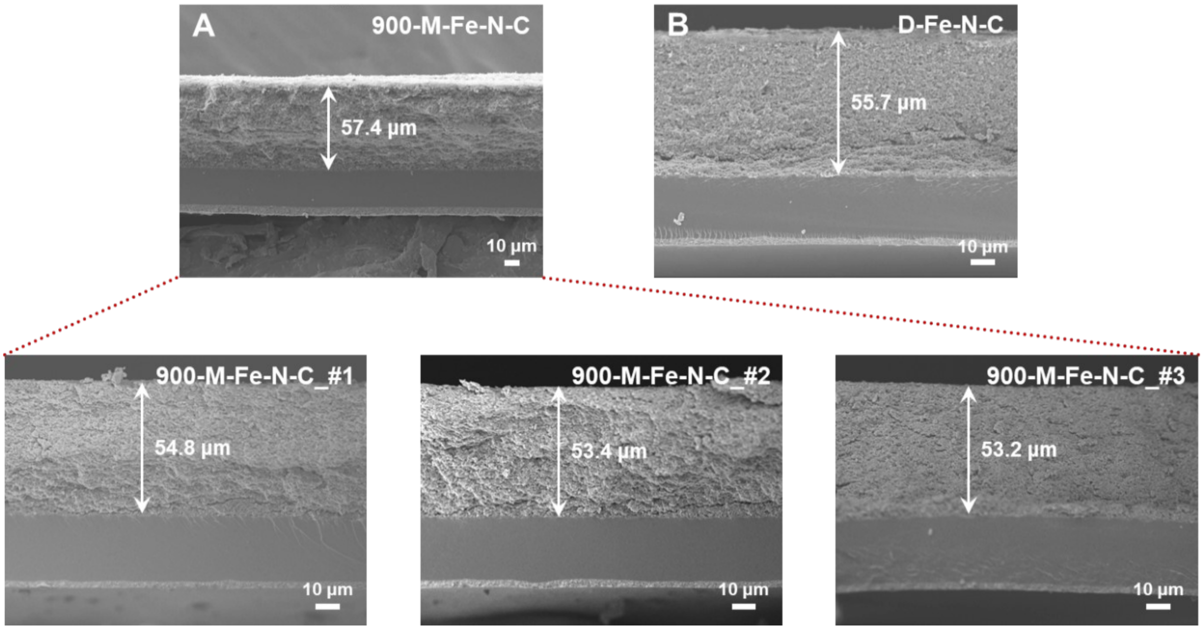

Fig. S24 Cross-sectional SEM images of (A) MEA with 900 M–Fe–N–C cathode and (B) MEA with D–Fe–N–C cathode.

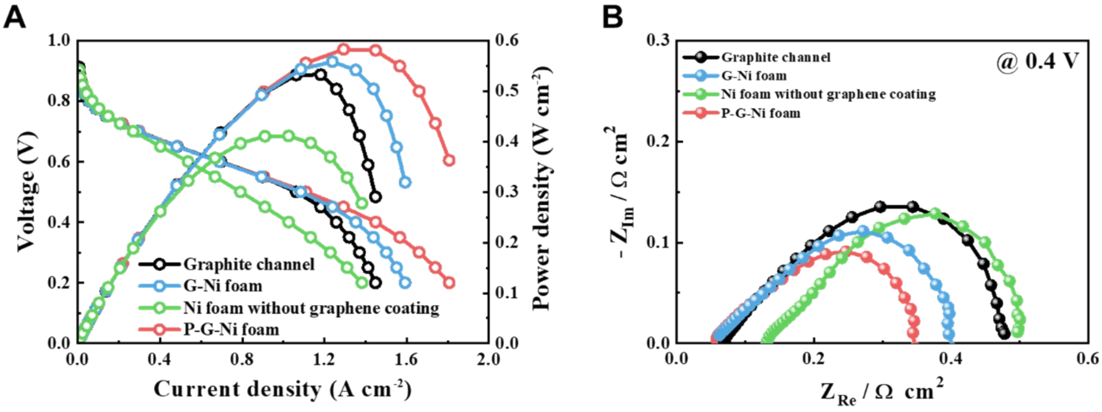

Fig. S25 (A) Polarization curves of the 900 M–Fe–N–C catalyst based MEA with various Ni foam applications at 80°C supplied with H_2/Air at 95% RH. (B) Corresponding EIS spectra at 0.4 V.

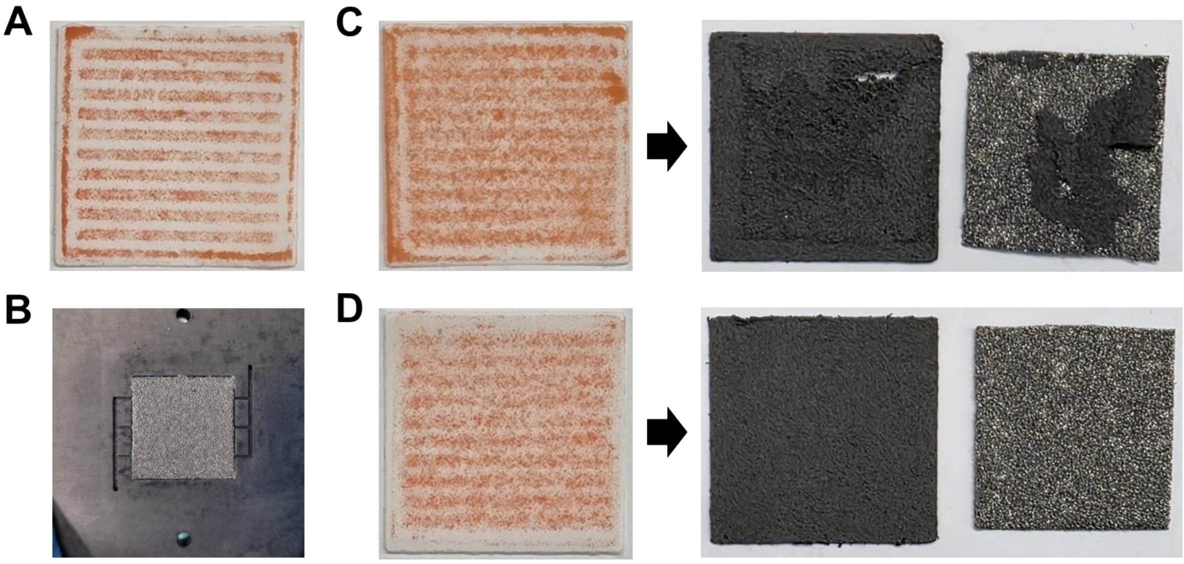

Fig. S26 (A) Pressure-sensitive film image obtained with the serpentine channel. (B) Ni foam flow field. (C) Pressure-sensitive film and GDL images with the uncompressed Ni foam. (D) Pressure-sensitive film and GDL images with the pre-compressed Ni foam.

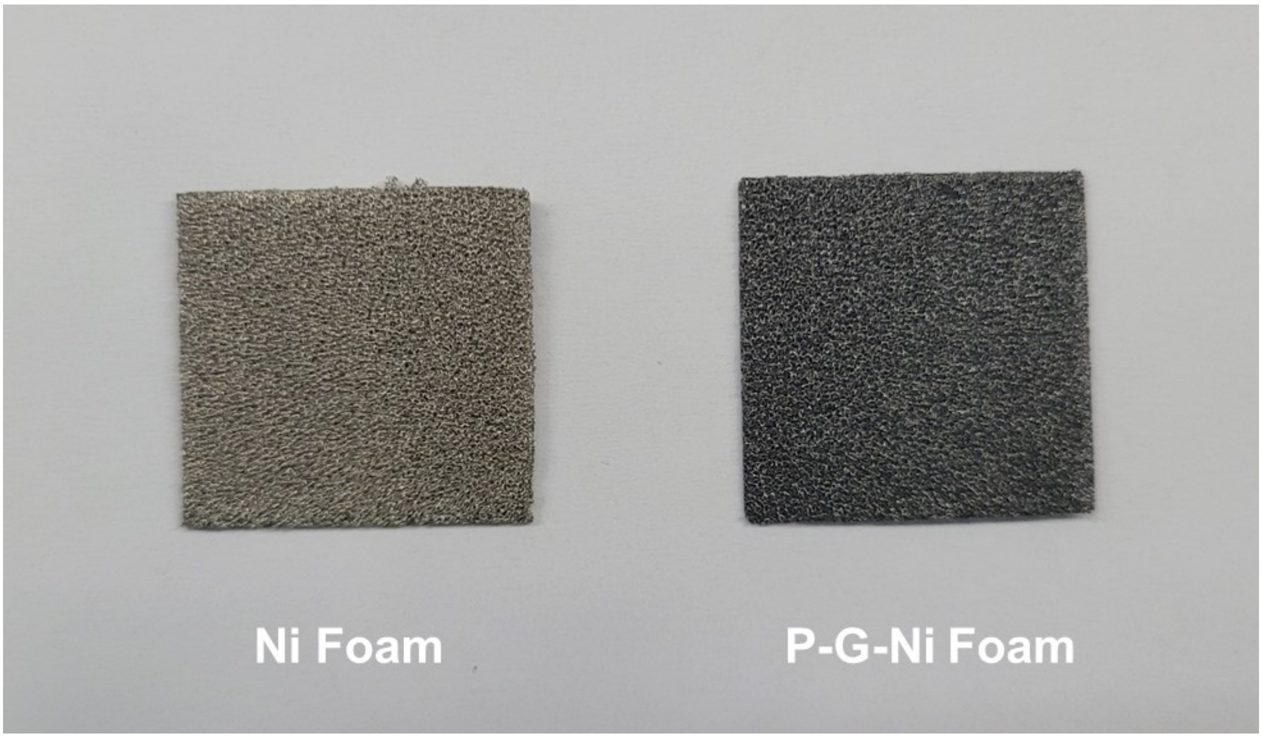

Fig. S27 Digital images of pure Ni foam and P–G–Ni foam.

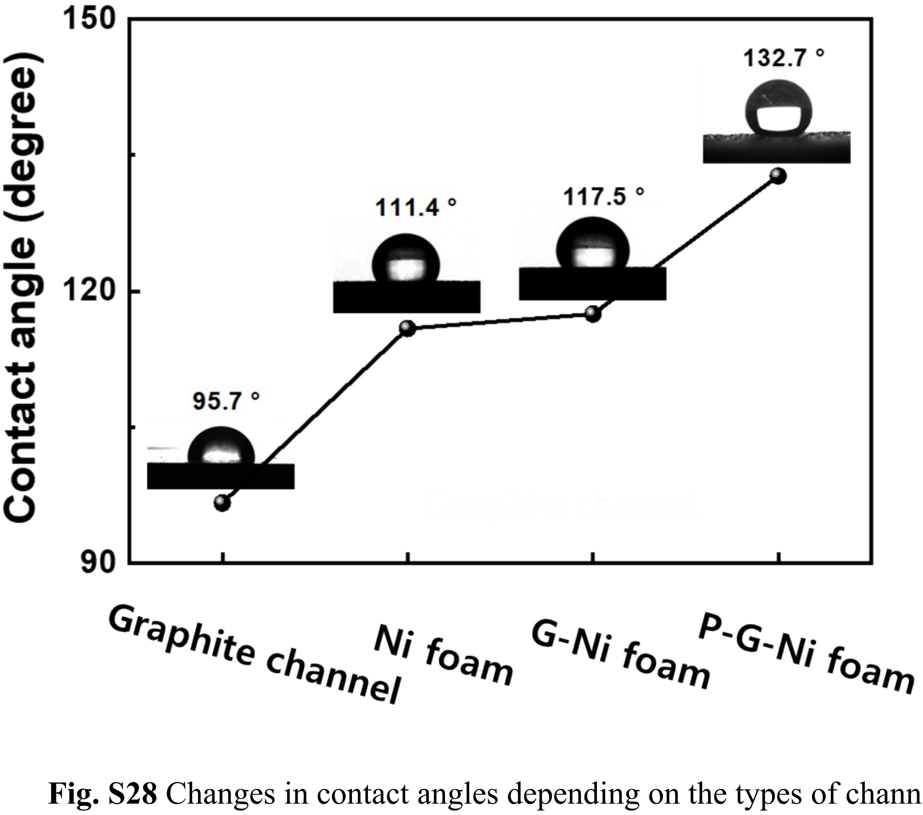

Fig. S28 Changes in contact angles depending on the types of channels.

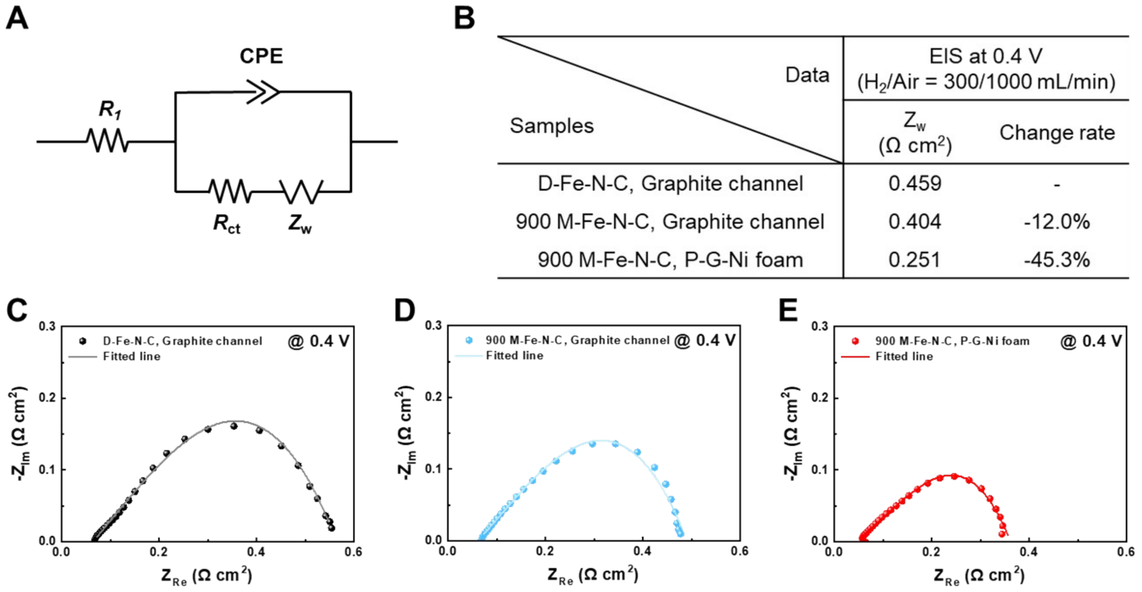

Data / Samples	EIS at 0.4 V (H_2/Air = 300/1000 mL/min)	
	Z_w (Ω cm^2)	Change rate
D-Fe-N-C, Graphite channel	0.459	-
900 M-Fe-N-C, Graphite channel	0.404	-12.0%
900 M-Fe-N-C, P-G-Ni foam	0.251	-45.3%

Fig. S29 (A) Randles-Ershler equivalent circuit model for cathodic reaction of the PEMFC (R_1 = membrane resistance, R_{ct}= charge transfer resistance, CPE = constant phase element of the cathode and Z_w = Warburg impedance). (B) Warburg impedance according to catalyst and flow field. (C) EIS fitting for D–Fe–N–C with Graphite channel. (D) EIS fitting for 900 M–Fe–N–C with Graphite channel. (E) EIS fitting for 900 M–Fe–N–C with P–G–Ni foam.

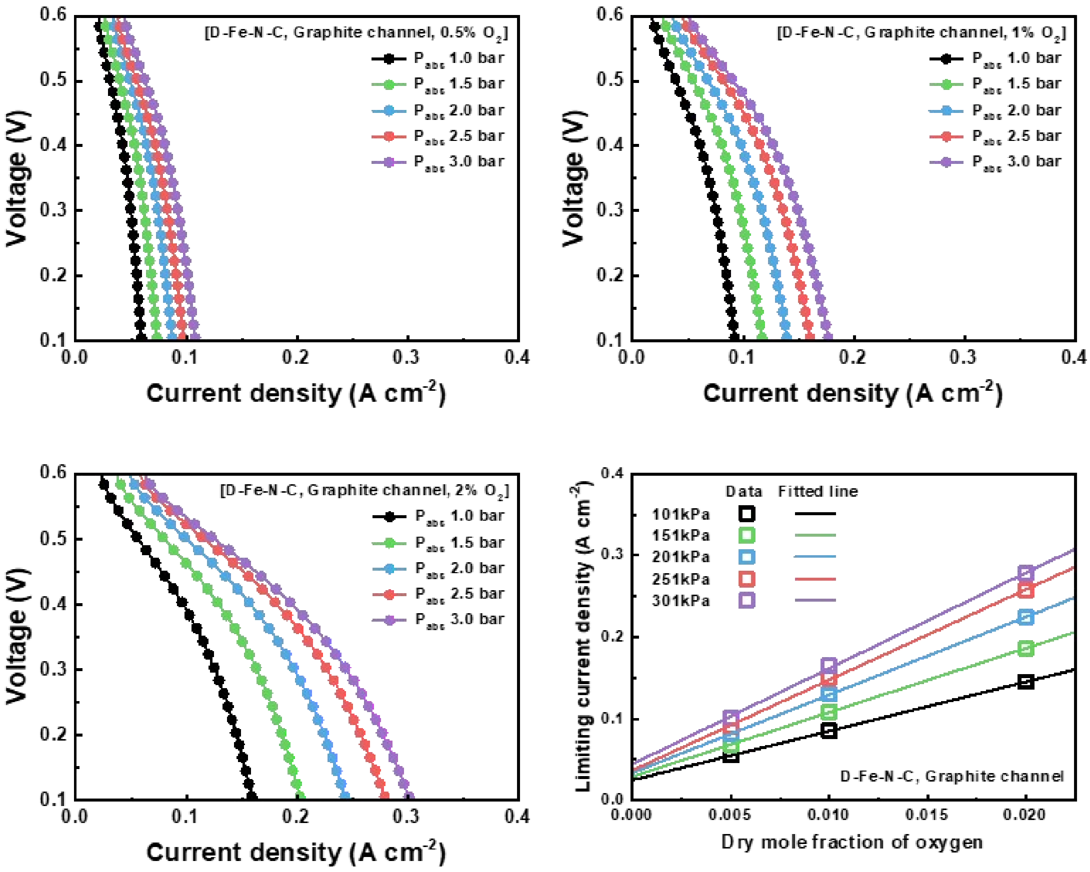

Fig. S30 Voltage-current density curves for each mole fraction of oxygen at different total gas pressures for D–Fe–N–C catalyst.

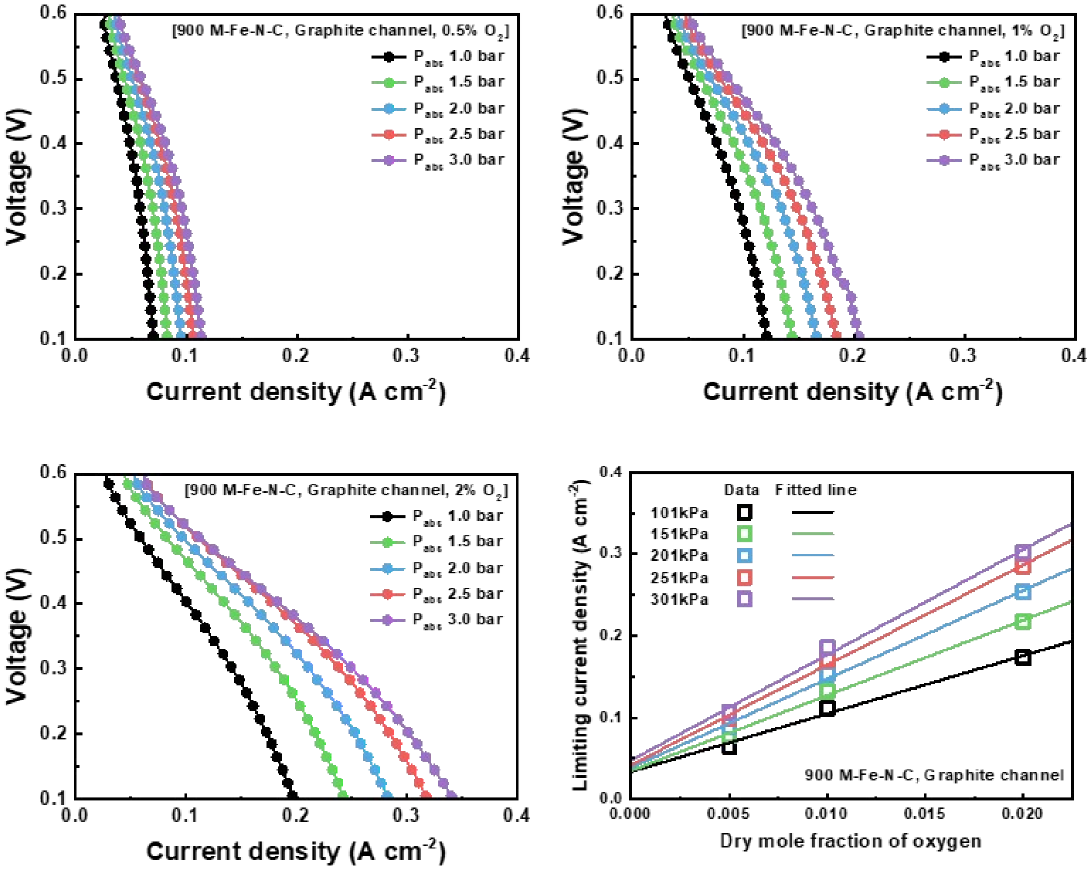

Fig. S31 Voltage-current density curves for each mole fraction of oxygen at different total gas pressures for 900 M–Fe–N–C catalyst.

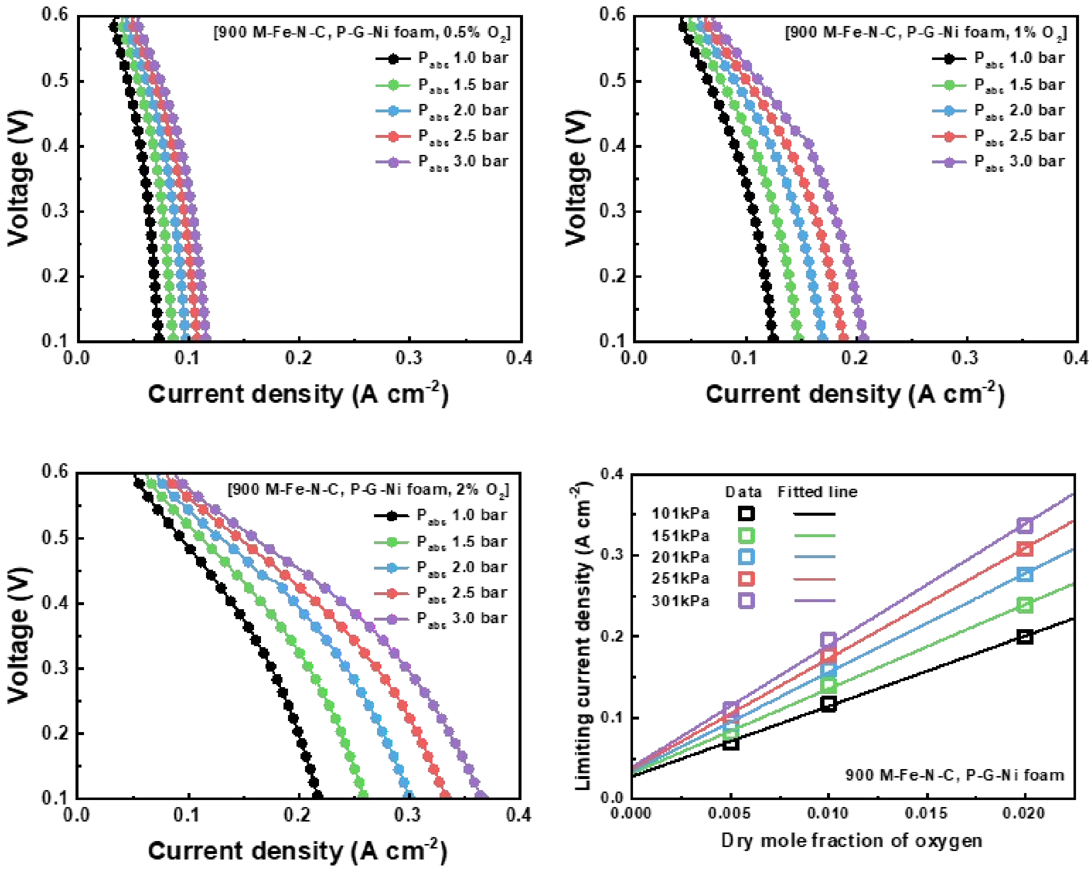

Fig. S32 Voltage-current density curves for each mole fraction of oxygen at different total gas pressures for 900 M–Fe–N–C catalyst with P–G–Ni foam.

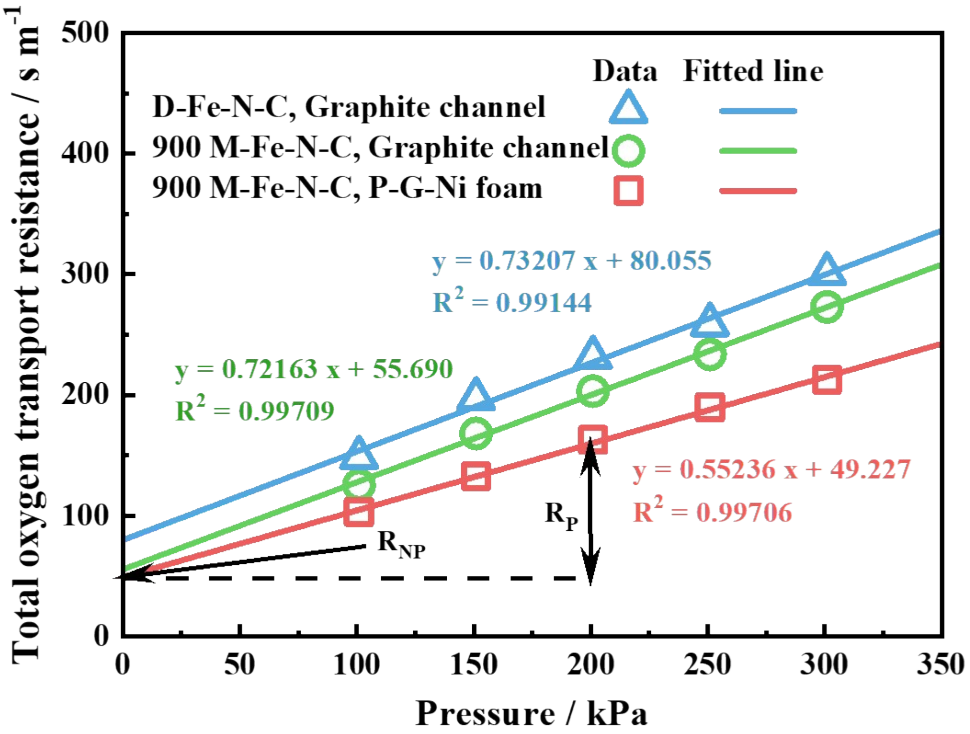

Fig. S33 Total oxygen transport resistance of the cells.

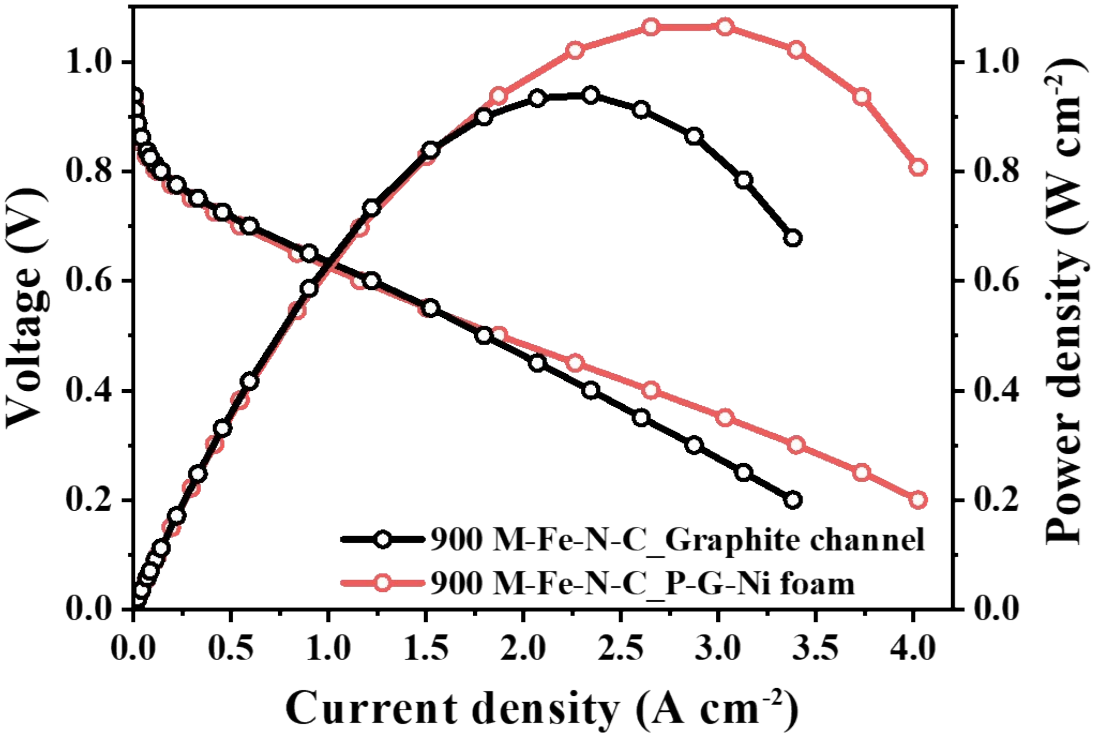

Fig. S34 Polarization curves of the MEAs with P–G–Ni foam as the flow field on the cathode side under H_2/O_2 conditions.

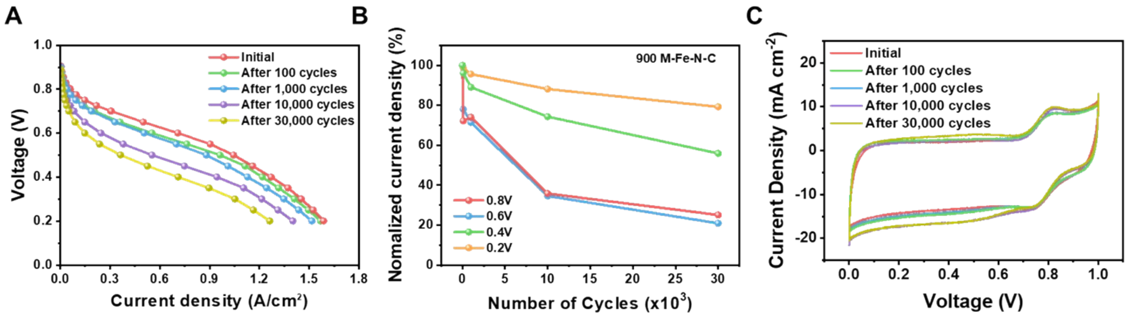

Samples \ Data	PPD (W cm^{-2})	Normalized current density (%)				Capacitance (mF cm^{-2})
		0.8 V	0.6 V	0.4 V	0.2 V	
Initial	0.523	100	100	100	100	382.1
100 cycles	0.502	72.2	78.0	96.1	98.7	404.0
1000 cycles	0.455	74.0	71.4	89.0	95.6	399.9
10000 cycles	0.388	35.8	34.6	74.3	88.1	432.0
30000 cycles	0.316	25.1	20.9	55.9	79.2	446.5

Fig. S35 (A) Performance degradation of 900 M–Fe–N–C during cycling at different voltages. (B) Normalized current density degradation during cycling at 0.8, 0.6, 0.4, and 0.2 V, measured under H_2/air conditions for 900 M–Fe–N–C. (C) Changes in the CV spectra during cycling under H_2/N_2 conditions.

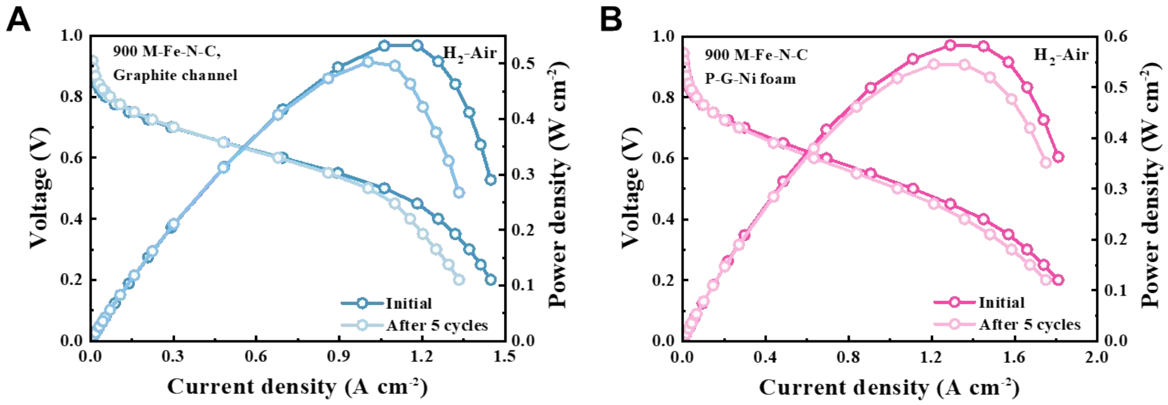

Fig. S36 The performance of 900 M–Fe–N–C at initial state and after 5 cycles: (A) Graphite channel. (B) P-G-Ni foam.

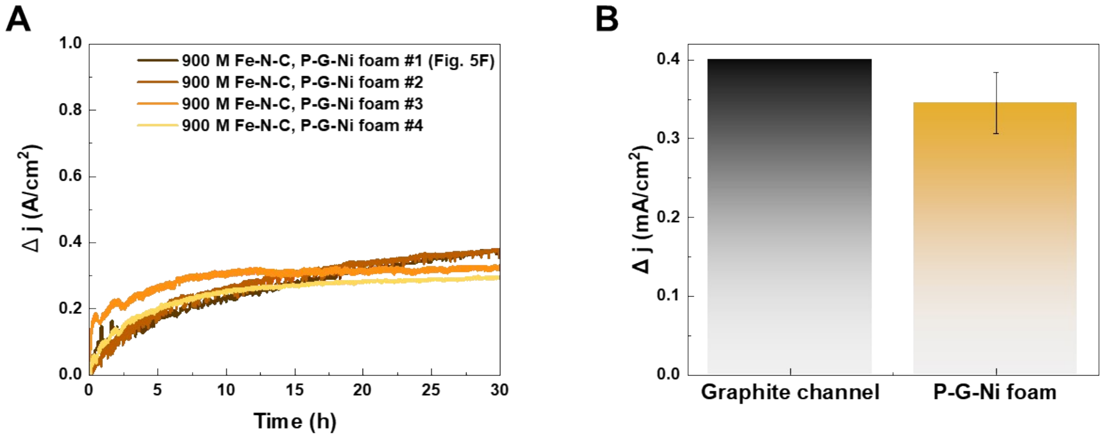

Fig. S37 (A) Current density loss of P–G–Ni foam during the 30-hour durability test (@0.5 V). (B) Standard deviation of current density loss of P-G-Ni foam.

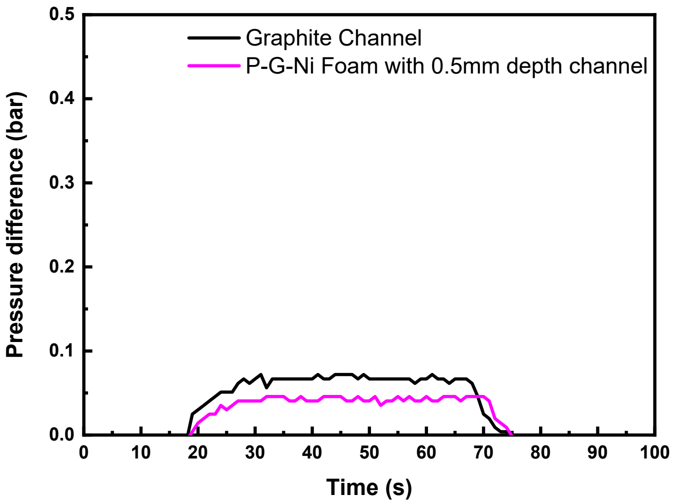

Fig. S38 Pressure drop between the inlet and outlet for the graphite channel and the P–G–Ni foam.

Supplementary Tables

Table S1. Elemental quantification of Fe–N–C catalysts determined by XPS (at%)

	C (at%)	N (at%)	O (at%)	Fe (at%)
D-Fe-N-C	89.26	5.46	5.03	0.25
DM-Fe-N-C	88.4	6.03	5.27	0.3
1000 M-Fe-N-C	89.29	5.4	5.01	0.3
900 M-Fe-N-C	89.19	5.72	4.85	0.24
800 M-Fe-N-C	88.44	6.51	4.72	0.33
700 M-Fe-N-C	88.27	6.54	4.96	0.23

Table S2. Elemental quantification of nitrogen species Fe–N–C catalysts determined by XPS (Figure S10)

N species (%)	Graphitic-N	Pyridinic-N	Pyrrolic-N	Fe-N_x	Oxidized-N
D-Fe-N-C	33	33.25	2.81	2.76	28.18
DM-Fe-N-C	32.32	36.33	2.53	2.39	26.43
1000 M-Fe-N-C	33.61	36.53	2.92	2.71	24.23
900 M-Fe-N-C	34.05	39.46	2.65	2.69	21.14
800 M-Fe-N-C	32.22	42.39	2.76	2.61	20.46
700 M-Fe-N-C	32.04	43.14	2.92	2.65	19.26

Table S3. Fe elemental quantification of Fe–N–C catalysts determined by ICP-OES (wt%)

Sample	D-Fe-N-C	DM-Fe-N-C	1000 M-Fe-N-C
Fe (wt%)	1.77	1.74	1.7
Sample	**900 M-Fe-N-C**	**800 M-Fe-N-C**	**700 M-Fe-N-C**
Fe (wt%)	1.66	1.73	1.68

Table S4. EXAFS results for Fe–N–C catalysts. CN: coordination number; R: interatomic distance; σ^2: Debye-Waller factor that is related to thermal and static disorder in absorber-scatterer distances; ΔE_0: edge-energy shift; R-factor: represents goodness of the fitting; the amplitude reduction factor S_0^2 was determined to be 0.87 obtained using Fe foil fitting as a reference.

	Path	CN	R(Å)	σ^2(Å^2)	ΔE_0 (eV)	R factor (%)
D-Fe-N-C	**Fe-N/O**	**4.86**	**2.006(2)**	**0.006(4)**	**9.4**	**0.24**
DM-Fe-N-C		**4.7**	**1.996(3)**	**0.007(8)**	**8.5**	**0.29**
1000 M-Fe-N-C		**4.85**	**1.994(2)**	**0.008(8)**	**8.35**	**0.23**
900 M-Fe-N-C		**4.81**	**1.997(6)**	**0.009(2)**	**8.85**	**0.46**
800 M-Fe-N-C		**4.88**	**1.998(2)**	**0.010(6)**	**8.65**	**0.71**
700 M-Fe-N-C		**4.8**	**1.999(8)**	**0.010(8)**	**8.88**	**1.04**

Table S5. RT ^{57}Fe Mössbauer spectra results of M–Fe–N–C catalysts and parameters derived from the fittings. Quadrupole splitting (QS), Isomer shift (IS), line width (fwhm) of each component.

Sample		**1000 M-Fe-N-C**	**900 M-Fe-N-C**	**800 M-Fe-N-C**	**700 M-Fe-N-C**	**Assignment**
D1	QS (mm/s)	1	1	0.95	0.9	**High spin Fe^{3+}N$_4$**
	IS (mm/s)	0.22	0.18	0.17	0.24	
	fwhm (mm/s)	0.67	0.7	0.65	0.65	
D2	QS (mm/s)	2.59	2.59	2.5	2.45	**Low or Intermediate Spin Fe^{2+}N$_4$**
	IS (mm/s)	0.28	0.18	0.18	0.15	
	fwhm (mm/s)	1.08	1.11	1.08	1.01	
D3	QS (mm/s)	2.65	2.8	2.72	2.85	**High spin Fe^{2+}N$_4$**
	IS (mm/s)	1.05	1.1	1.05	1.05	
	fwhm (mm/s)	0.9	0.9	0.9	0.9	
Area (%)	**D1**	63.47	67	68.22	70.73	
	D2	28.27	25.6	24.78	24	
	D3	8.26	7.4	7	5.37	

Table S6. Theoretical calculation results of Fe–N bond length varying local strain on Fe–N_4 active sites.

Local strain (%)	0.421 %	0.000 %	-0.210 %	-0.631%	-1.577%
Fe-N bond length (Å)	1.910	1.902	1.898	1.890	1.872

Table S7. Comparison of single cell performance of 900 M–Fe–N–C with other reported PGM-free catalysts

Catalyst	Temperature [℃]	Flow rate [mL min^{-1}]	Peak power density [W cm^{-2}]		Cathode loading [mg cm^{-2}]	Reference
			H_2/O_2	H_2/air		
900 M-Fe-N-C	80	300/1000	0.939 (1.0 bar)	0.533 (1.0 bar)	3.0	This work
900 M-Fe-N-C P-G-Ni foam	80	300/1000	1.06 (1.0 bar)	0.583 (1.0 bar)	3.0	This work
(CM+PANI)-Fe-C	80	200/760	0.87 (1.0 bar)	0.42 (1.0 bar)	4.0	[18]
Fe SAC-MOF-5	80	250/350	0.84 (2.0 bar)	0.31 (1.0 bar)	4.0	[19]
Fe/NC-NaCl	NA	150/200	0.89 (1.0 bar)	0.39 (1.0 bar)	4.0	[20]
Fe_{SA}/Fe_{Ac}-2DNPC	80	300/400 (H_2/O_2) 300/600 (H_2/air)	0.94 (2.0 bar)	0.34 (1.0 bar)	1.5	[21]
FeNC-CVD-750	80	200/1000 (H_2/O_2) 500/2000 (H_2/air)	0.59 (1.0 bar)	0.37 (1.0 bar)	6.0	[22]
Fe-MOF	94	200/1000	1.14 (1.7 bar)	0.61 (1.7 bar)	4.0	[23]
Fe/Zr-N-C	80	300/300 (H_2/O_2) 300/600 (H_2/air)	1.20 (2.0 bar)	0.72 (2.0 bar)	2.0	[24]
Fe SAs/N-C	80	NA	0.75 (2.0 bar)	0.35 (2.0 bar)	1.5	[25]
FeAl-RNC	80	300/300 (H_2/O_2) 300/1500 (H_2/air)	1.05 (1.5 bar)	0.60 (1.5 bar)	4.0	[26]
FeN_X/GM	80	300/300	0.86 (20 psi)	0.43 (20 psi)	4.0	[27]
Fe-N-C-Phen-PANI	80	300/400	1.06 (20 psi)	0.38 (20 psi)	4.0	[28]
FeN_4/HOPC-c-1000	80	200/200 (H_2/O_2) 200/300 (H_2/air)	0.69 (1.0 bar)	0.42 (1.0 bar)	4.0	[29]
1.5Fe-ZIF	80	200/200	0.67 (1.0 bar)	0.36 (1.0 bar)	4.0	[30]
Sur-FeN_4-HPC	80	300/500	0.79 (1.0 bar)	0.412 (1.0 bar)	4.0	[31]
Fe-NC$^{\Delta\text{-DCDA}}$	80	200/200 (H_2/O_2) 300/1000 (H_2/air)	>0.78 (1.0 bar)	0.429 (1.0 bar)	3.9	[32]

Table S8. Comparison of single cell durability of 900 M–Fe–N–C with other reported PGM-free catalysts.

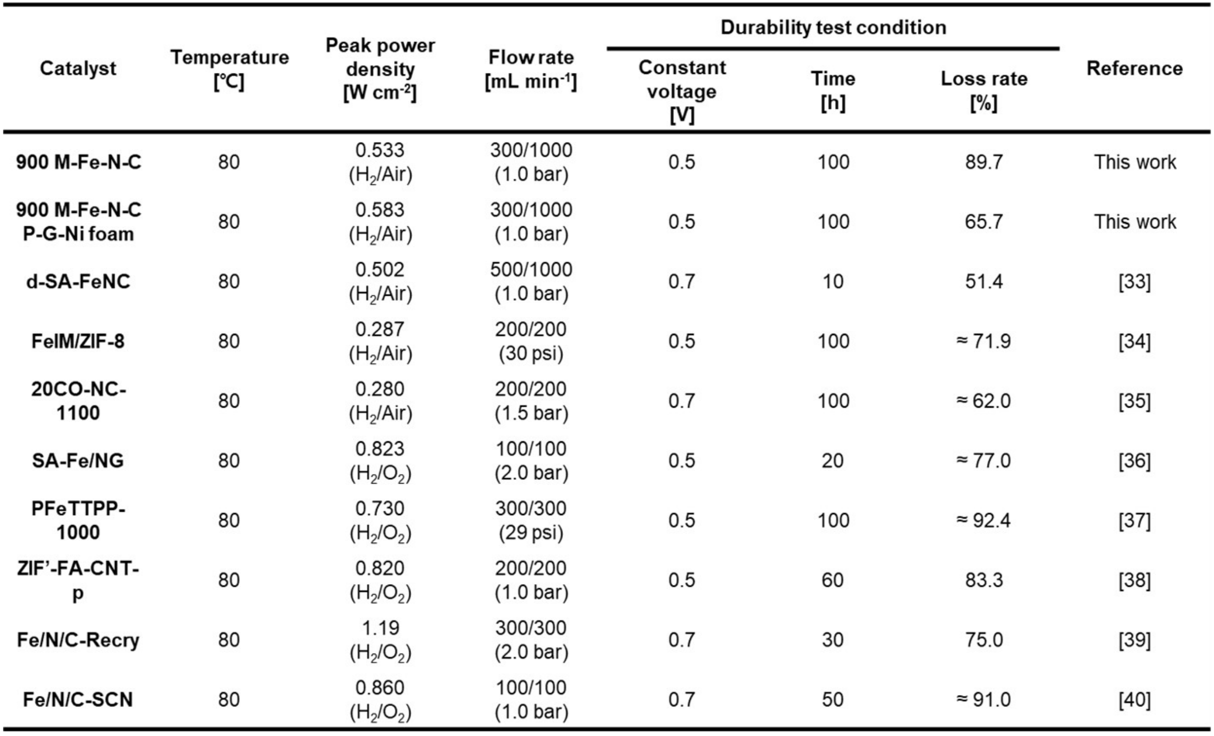

Catalyst	Temperature [℃]	Peak power density [W cm^{-2}]	Flow rate [mL min^{-1}]	Durability test condition			Reference
				Constant voltage [V]	Time [h]	Loss rate [%]	
900 M-Fe-N-C	80	0.533 (H_2/Air)	300/1000 (1.0 bar)	0.5	100	89.7	This work
900 M-Fe-N-C P-G-Ni foam	80	0.583 (H_2/Air)	300/1000 (1.0 bar)	0.5	100	65.7	This work
d-SA-FeNC	80	0.502 (H_2/Air)	500/1000 (1.0 bar)	0.7	10	51.4	[33]
FeIM/ZIF-8	80	0.287 (H_2/Air)	200/200 (30 psi)	0.5	100	≈ 71.9	[34]
20CO-NC-1100	80	0.280 (H_2/Air)	200/200 (1.5 bar)	0.7	100	≈ 62.0	[35]
SA-Fe/NG	80	0.823 (H_2/O_2)	100/100 (2.0 bar)	0.5	20	≈ 77.0	[36]
PFeTTPP-1000	80	0.730 (H_2/O_2)	300/300 (29 psi)	0.5	100	≈ 92.4	[37]
ZIF'-FA-CNT-p	80	0.820 (H_2/O_2)	200/200 (1.0 bar)	0.5	60	83.3	[38]
Fe/N/C-Recry	80	1.19 (H_2/O_2)	300/300 (2.0 bar)	0.7	30	75.0	[39]
Fe/N/C-SCN	80	0.860 (H_2/O_2)	100/100 (1.0 bar)	0.7	50	≈ 91.0	[40]

Supplementary Reference

1. D. Malko, A. Kucernak and T. Lopes, *Nat. Commun.*, 2016, 7, 13285.

2. P. P. Lopes, D. Strmcnik, D. Tripkovic, J. G. Connell, V. Stamenkovic and N. M. Markovic, *ACS Catal.*, 2016, 6, 2536-2544.

3. G. Kresse and J. Furthmüller, *Comput. Mater. Sci.*, 1996, **6**, 15-50.

4. P. E. Blöchl, *Phys. Rev. B*, 1994, **50**, 17953.

5. J. P. Perdew, K. Burke and M. Ernzerhof, *Phys. Rev. Lett.*, 1996, **77**, 3865.

6. S. Grimme, *J. Comput. Chem.*, 2006, **27**, 1787-1799.

7. S. Grimme, J. Antony, S. Ehrlich and H. Krieg, *J. Chem. Phys.*, 2010, **132**.

8. K. Mathew, R. Sundararaman, K. Letchworth-Weaver, T. Arias and R. G. Hennig, *J. Chem. Phys.*, 2014, **140**.

9. A. H. Larsen, J. J. Mortensen, J. Blomqvist, I. E. Castelli, R. Christensen, M. Dułak, J. Friis, M. N. Groves, B. Hammer and C. Hargus, *J. Phys. Condens. Matter*, 2017, **29**, 273002.

10. A. Kulkarni, S. Siahrostami, A. Patel and J. K. Nørskov, *Chem. Rev.*, 2018, **118**, 2302-2312.

11. V. L. Deringer, A. L. Tchougréeff and R. Dronskowski, *J. Phys. Chem. A*, 2011, **115**, 5461-5466.

12. S. Maintz, V. L. Deringer, A. L. Tchougréeff and R. Dronskowski, *J. Comput. Chem. 2016, 37, 1030–1035.*

13. T. Patniboon and H. A. Hansen, *ACS Catal.*, 2021, **11**, 13102-13118.

14. S. Liu, C. Li, M. J. Zachman, Y. Zeng, H. Yu, B. Li, M. Wang, J. Braaten, J. Liu and H. M. Meyer III, *Nat. Energy*, 2022, **7**, 652-663.

15. S. G. Bratsch, *J. Phys. Chem. Ref. Data*, 1989, **18**, 1-21.

16. J. Choi, D. Kim, J. E. Chae, S. Lee, S. M. Kim, S. J. Yoo, H.-J. Kim, M. Choi and S. Jang, *ACS Appl. Mater. Interfaces*, 2022, **14**, 50956-50965.

17. S. Y. Yi, E. Choi, H. Y. Jang, S. Lee, J. Park, D. Choi, Y. Jang, H. Kang, S. Back and S. Jang, *Adv. Mater.*, 2023, **35**, 2302666.

18. H. T. Chung, D. A. Cullen, D. Higgins, B. T. Sneed, E. F. Holby, K. L. More and P. Zelenay, *Science*, 2017, **357**, 479-484.

19. X. Xie, L. Shang, X. Xiong, R. Shi and T. Zhang, *Adv. Energy Mater.*, 2022, **12**, 2102688.

20. Q. Wang, Y. Yang, F. Sun, G. Chen, J. Wang, L. Peng, W. T. Chen, L. Shang, J. Zhao, D. Sun-Waterhouse, T. Zhang and G. I. N. Waterhouse, *Adv. Energy Mater.*, 2021, **11**, 2100219.

21. X. Wan, Q. Liu, J. Liu, S. Liu, X. Liu, L. Zheng, J. Shang, R. Yu and J. Shui, *Nat. Commun.*, 2022, **13**, 2963.

22. L. Jiao, J. Li, L. L. Richard, Q. Sun, T. Stracensky, E. Liu, M. T. Sougrati, Z. Zhao, F. Yang, S. Zhong, H. Xu, S. Mukerjee, Y. Huang, D. A. Cullen, J. H. Park, M. Ferrandon, D. J. Myers, F. Jaouen, Q. Jia, *Nat. Mater.*, 2021, **20**, 1385-1391.

23. A. Uddin, L. Dunsmore, H. Zhang, L. Hu, G. Wu and S. Litster, *ACS Appl. Mater. Interfaces*, 2019, **12**, 2216-2224.

24. B. Chi, L. Zhang, X. Yang, Y. Zeng, Y. Deng, M. Liu, J. Huo, C. Li, X. Zhang, X. Shi, Y. Shao, L. Gu, L. Zheng, Z. Cui, S. Liao and G. Wu, *ACS Catal.*, 2023, **13**, 4221-4230.

25. Z. Yang, Y. Wang, M. Zhu, Z. Li, W. Chen, W. Wei, T. Yuan, Y. Qu, Q. Xu, C. Zhao, X. Wang, P. Li, Y. Li, Y. Wu and Y. Li, *ACS Catal.*, 2019, **9**, 2158-2163.

26. Y. Liu, J. Li, Z. Lv, H. Fan, F. Dong, C. Wang, X. Chen, R. Liu, C. Tian, X. Feng, W. Yang and B. Wang, *J. Am. Chem. Soc.*, 2024, **146**, 12636-12644.

27. X. Fu, N. Li, B. Ren, G. Jiang, Y. Liu, F. M. Hassan, D. Su, J. Zhu, L. Yang, Z. Bai, Z. P. Cano, A. Yu, Z. Chen, *Adv. Energy Mater.*, 2019, **9**, 1803737.

28. X. Fu, P. Zamani, J.-Y. Choi, F. M. Hassan, G. Jiang, D. C. Higgins, Y. Zhang, M. A. Hoque and Z. Chen, *Adv. Mater*, 2017, **29**, 1604456.

29. M. Qiao, Y. Wang, Q. Wang, G. Hu, X. Mamat, S. Zhang and S. Wang, *Angew. Chem. Int. Ed.*, 2020, **59**, 2688-2694.

30. H. Zhang, H. T. Chung, D. A. Cullen, S. Wagner, U. I. Kramm, K. L. More, P. Zelenay and G. Wu, *Energy Environ. Sci.*, 2019, **12**, 2548-2558.

31. G. Chen, Y. An, S. Liu, F. Sun, H. Qi, H. Wu, Y. He, P. Liu, R. Shi, J. Zhang, A. Kuc, U. Kaiser, T. Zhang, T. Heine, G. Wu and X. Feng, *Energy Environ. Sci.*, 2022, **15**, 2619-2628.

32. A. Mehmood, M. Gong, F. Jaouen, A. Roy, A. Zitolo, A. Khan, M.-T. Sougrati, M. Primbs, A. M. Bonastre, D. Fongalland, G. Drazic, P. Strasser and A. Kucernak, *Nat. Catal.*, 2022, **5**, 311-323.

33. L. Shi, X. Lin, F. Liu, Y. Long, R. Cheng, C. Tan, L. Yang, C. Hu, S. Zhao and D. Liu, *ACS Catal.*, 2022, **12**, 5397-5406.

34. D. Zhao, J.-L. Shui, C. Chen, X. Chen, B. M. Reprogle, D. Wang and D.-J. Liu, *Chem. Sci.*, 2012, **3**, 3200-3205.

35. X. X. Wang, D. A. Cullen, Y. T. Pan, S. Hwang, M. Wang, Z. Feng, J. Wang, M. H. Engelhard, H. Zhang, Y. He, Y. Shao, D. Su, K. L. More, J. S. Spendelow and G. Wu *Adv. Mater.*, 2018, **30**, 1706758.

36. L. Yang, D. Cheng, H. Xu, X. Zeng, X. Wan, J. Shui, Z. Xiang and D. Cao, *Proc. Natl. Acad. Sci. U.S.A.*, 2018, **115**, 6626-6631.

37. S. Yuan, J. L. Shui, L. Grabstanowicz, C. Chen, S. Commet, B. Reprogle, T. Xu, L. Yu and D. J. Liu, *Angew. Chem. Int. Ed.*, 2013, **52**.

38. C. Zhang, Y. C. Wang, B. An, R. Huang, C. Wang, Z. Zhou and W. Lin, *Adv. Mater.*, 2017, **29**, 1604556.

39. Y. Wu, M. Yuan, X. Li, R. Ding, X. Duan, J. Li, Y. Wang, X. Li, Y. Zhang and J. Liu, *Appl. Catal. B: Environ.*, 2022, **312**, 121365.

40. J. Zhu, Z. Fang, X. Yang, M. Chen, Z. Chen, F. Qiu, M. Wang, P. Liu, Q. Xu and X. Zhuang and G. Wu, *ACS Catal.*, 2022, **12**, 6409-6417.